Spherical orbits around Kerr-Newman and Ghosh black holes

A. S. Alam,[*] L. C. Andaru,[†] B. N. Jayawiguna[‡],[§] and H. S. Ramadhan[¶][**]

Departemen Fisika, FMIPA, Universitas Indonesia, Depok, 16424, Indonesia.

Abstract

We conduct a comprehensive study on spherical orbits around two types of black holes: Kerr-Newman black holes, which are charged, and Ghosh black holes, which are nonsingular. In this work, we consider both null and timelike cases of orbits. Utilizing the Mino formalism, all analytical solutions for the geodesics governing these orbits can be obtained. It turns out that all spherical photon orbits outside the black hole horizons are unstable. In the extremal cases of both models, we obtain the *photon boomerangs*. The existence of charge in the Kerr-Newman allows the orbits to transition between retrograde and prograde motions, and its increase tends to force the orbits to be more equatorial. On the other hand, the Ghosh black hole, characterized by a regular core and a lack of horizons in certain conditions, presents the possibility of observable stable spherical orbits in the so-called *no-horizon* condition. As the Ghosh parameter k increases, trajectories tend to exhibit larger latitudinal oscillation amplitudes. We observe that as the Ghosh parameter k increases the trajectories tend to have larger latitudinal oscillation amplitudes. Finally, we investigate the existence of *innermost stable spherical orbits* (ISSOs). Both black holes demonstrate the appearance of two branches of ISSO radii as a function of the Carter constant C. However, there are notable differences in their behavior: in the case of the Kerr-Newman black hole, the branches merge at a critical value, beyond which no ISSO exists, while for the Ghosh black hole, the transcendental nature of the metric function causes the branches to become complex at some finite distance.

[‡] Present Address: High Energy Physics Theory Group, Department of Physics, Faculty of Science, Chulalongkorn University, Bangkok 10330, Thailand.

[¶] Corresponding author.

[*]Electronic address: agya.sewara@ui.ac.id

[†]Electronic address: langga.calvareno@ui.ac.id

[§]Electronic address: byon.nugraha91@ui.ac.id

[**]Electronic address: hramad@sci.ui.ac.id

I. INTRODUCTION

It is well-known that any system possessing spherical symmetry and staticity will preserve its angular momentum, and as a result, the corresponding dynamics are confined on a plane. This is true in classical mechanics as well as in general relativity (GR). What is genuine in GR, among other things, is that not only massive particles but light can also orbit around a massive object. Perhaps the ultimate massive object in the universe is a black hole. Its visual image was first released in 2019 by the Event Horizon Telescope (EHT) collaboration [1] for M87*, and for Sgr A* three years later [2]. For Schwarzschild we know that the photon circular orbit (*photon sphere*, r_{ps}) is $r_{ps} = 3M$ [3], while for Reissner-Nordstrom (RN) there are $r_{ps}^{\pm} = 3/2 \left(M \pm \sqrt{M^2 - 8Q^2/9} \right)$ [4, 5]. Both the Schwarzschild and RN unstable photon spheres are outside their corresponding shadow radii [6–11], thus can be observed. In reality, however, all astrophysical objects including black holes rotate. The appropriate metric solutions are the Kerr and the Kerr-Newman (KN) [12, 13]. EHT observed the Sgr A* angular diameter $d_{sh} = 48.7 \pm 7\mu as$, which exhibits consistency with theoretical predictions of Kerr black hole [2]. Moreover, the observation confirms that the Sgr A* shows the viability of the Kerr model with constrained charge (KN) [14–19].

The rotating metric introduces a departure from spherical symmetry, allowing for the existence of non-planar orbits, the *spherical orbits* (SO) being one of them. These orbits maintain a constant radius and trace the surface of a sphere. Their discovery stemmed from Carter's insight in 1968 [20], where he identified that rotation introduces an additional Killing tensor, leading to the conservation of a quantity known as "*Carter's constant*" C through Noether's theorem. Building upon this foundation, Wilkins in 1972 showcased the existence of "*spherical timelike orbits*" (STOs) in the extremal Kerr metric. Subsequently, Johnston and Ruffini extended these findings to the Kerr-Newman case [22].

The exploration of "*spherical photon orbits*" (SPO) began with Stuchlik's investigation of the Kerr model [23], followed by Calvani, De Felice, and Nobili's study of the Kerr-Newman scenario [24]. However, all studies on SPOs suggest that orbits are stable only within the inner horizon; beyond this region, they become inherently unstable. Nonetheless, SPOs play a crucial role in the observation of black holes. It is the multiple orbits of photon rays around black holes, terminated by their instability, that contribute to the formation of the luminous ring detected by instruments like the Event Horizon Telescope (EHT) [1, 2]. This

discovery holds significant implications for our understanding of black hole phenomena.

To determine the trajectory, one must solve geodesic equations with constant radii. The first numerical solutions were obtained by Goldstein [25]. Mino demonstrated in [26] that the geodesic equations can be decoupled, paving the way for Fujita and Hikida to achieve analytical solutions to the timelike geodesic equations in terms of elliptic integrals [27] (see also [28]). Further analytical investigations into Kerr(-Newman) geodesics can be found in works such as [29–32]. Teo leveraged this formalism to derive a one-parameter class of analytical solutions for spherical photon orbits [33] and timelike orbits [34]. These exact spherical orbits have been extensively explored in subsequent studies (see [35–38]).

Additionally for null trajectories, a family of parameters exists that causes the photon to return to the same point in the opposite direction after one azimuthal oscillation, satisfying the condition $\Delta \phi = \pi$. This phenomenon, termed the "photon boomerang," was introduced by Page [39]. In the case of Kerr black holes, it occurs in the near-extremal case, $a \approx 0.994M$, with zero angular momentum. Page demonstrated that the photon boomerang does not occur in naked singularities (NS) for pure Kerr. However, in [40], it was shown that a Kerr black hole surrounded by *perfect fluid dark matter* (PFDM) enables the existence of the photon boomerang under NS conditions. Related works on PFDM can be found in [41–47].

The singularity stands as one of the most generic and conceptually challenging aspects of black holes. However, it is widely believed that the singularity might be resolved or regularized within the framework of quantum gravity. The concept of a regular black hole devoid of a singularity was initially proposed by Sakharov [48] and later realized by Bardeen [49]. In the Bardeen metric, the near-core region exhibits behavior similar to the de Sitter space, and all invariants remain nonsingular throughout. Ayon-Beato and Garcia (ABG) demonstrated that the Bardeen metric can be derived from coupling Einstein's equations with a nonlinear electrodynamics (NLED) source [50, 51]. For an in-depth review of regular black holes, readers are referred to [52] and the accompanying references.

The concept of static regular black holes was subsequently extended to the rotating case by Bambi and Modesto [53], as well as by Toshmatov et al. [54] using the Newman-Janis algorithm. The resulting metrics are characterized by singularity-free Petrov type D solutions, although they suffer from violations of the weak energy condition. Ghosh [55] introduced a probability distribution function to mitigate these violations, resulting in a class of three-parameter stationary, symmetric metrics describing regular (nonsingular) rotating

black holes. These metrics depend on the mass (M), spin (a), and a free parameter (k) that quantifies the deviation from Kerr and generalizes the Kerr-Newman solution. Extensive literature discussing these solutions and their implications, including constraints from observations by the Event Horizon Telescope (EHT), can be found in [17, 56–59].

This paper aims to extensively explore the spherical orbit dynamics around Kerr-Newman and Ghosh black holes. In Section II, we delve into the behavior of spherical orbits around the Kerr-Newman (KN) black hole. We provide exhaustive analytical solutions and explicitly describe trajectories of the corresponding spherical photon orbits (SPOs) in Section II A, and spherical timelike orbits (STOs) in Section II B. Transitioning to Section III, we investigate the spherical orbit solutions of the (regular) Ghosh black hole. There, we present analytical solutions and conduct a thorough analysis of various types of SPOs and STOs trajectories in Section III A and Section III B, respectively. Finally, in Section IV, we synthesize and summarize our findings.

II. SPHERICAL ORBITS AROUND THE KERR-NEWMAN BLACK HOLE

The Kerr-Newman (KN) solutions in Boyer-Lindquist coordinate are [13]

$$ds^2 = -\frac{\Delta}{\Sigma} \left(dt - a\sin^2\theta d\phi\right)^2 + \frac{\sin^2\theta}{\Sigma} \left[\left(r^2 + a^2\right) d\phi - adt\right]^2 + \Sigma \left(\frac{dr^2}{\Delta} + d\theta^2\right), \quad (1)$$

and

$$A_\mu = \frac{Qr}{\Sigma} \left(1, 0, 0, -a\sin^2\theta\right), \quad (2)$$

where

$$\begin{aligned} \Sigma &\equiv r^2 + a^2\cos^2\theta, \\ \Delta &\equiv r^2 + a^2 - 2Mr + Q^2, \end{aligned} \quad (3)$$

and M, Q, a denote the black hole's mass, charge, and angular momentum per unit mass, respectively. The allowed range of a $0 < a^2 \leq M^2 - Q^2$, the upper and lower bounds of which are related to the extremal KN and the RN, respectively. The event horizons are $r_\pm \equiv M \pm \sqrt{M^2 - a^2 - Q^2}$. By defining $u \equiv \cos\theta$ the geodesic equations can be derived

using the Hamilton-Jacobi formalism [20, 22, 32]:

$$\Sigma \dot{t} = \left(\frac{r^2 + a^2}{\Delta}\right) P(r) - a \left[aE(1 - u^2) - L_z\right], \tag{4}$$

$$\Sigma \dot{r} = \sqrt{R(r)}, \tag{5}$$

$$\Sigma \dot{u} = \sqrt{\Theta(u)}, \tag{6}$$

$$\Sigma \dot{\phi} = \frac{a}{\Delta} P - \left(aE - \frac{L_z}{1 - u^2}\right), \tag{7}$$

with

$$R(r) \equiv P(r) - \Delta[\mathcal{C} + \mu^2 r^2 + (L_z - aE)^2],$$

$$\Theta(u) \equiv \mathcal{C} - \left[\mathcal{C} + L_z^2 + a^2(\mu^2 - E^2)\right] u^2 + a^2(\mu^2 - E^2)u^4, \tag{8}$$

$$P(r) \equiv \left[E(r^2 + a^2) - aL_z\right]^2.$$

The photon (/timelike) case appears when $\mu = 0$ (/$\mu = 1$). The dot refers to the derivative wrt the Affine parameter τ, $\mathcal{C}$ is the Carter's constant, E and L_z are the energy and angular momentum about ϕ-axis of the photon, respectively.

A. Spherical Photon Orbits

The SPO conditions are Eqs. (4)-(8) with $\mu = 0$. The solutions for Eq. (6) are physical whenever $\Theta(u) \geq 0$. The bounds of u values are the roots of $\Theta(u_0) = 0$. Since $\Theta(u)$ is not Q-dependent, the roots are exactly the same as in the Kerr case [33, 34]. Defining

$$\Phi \equiv \frac{L_z}{E}, \qquad C \equiv \frac{\mathcal{C}}{E^2}, \tag{9}$$

we have, for $C > 0$,

$$u_0^2 = \frac{(a^2 - C - \Phi^2) + \sqrt{(a^2 - C - \Phi^2)^2 + 4a^2 C}}{2a^2}. \tag{10}$$

When $C < 0$, the following condition must be satisfied

$$a^2 - C - \Phi^2 > 0. \tag{11}$$

The spherical orbit condition requires the corresponding radius ($\equiv r_{SO}$) satisfies

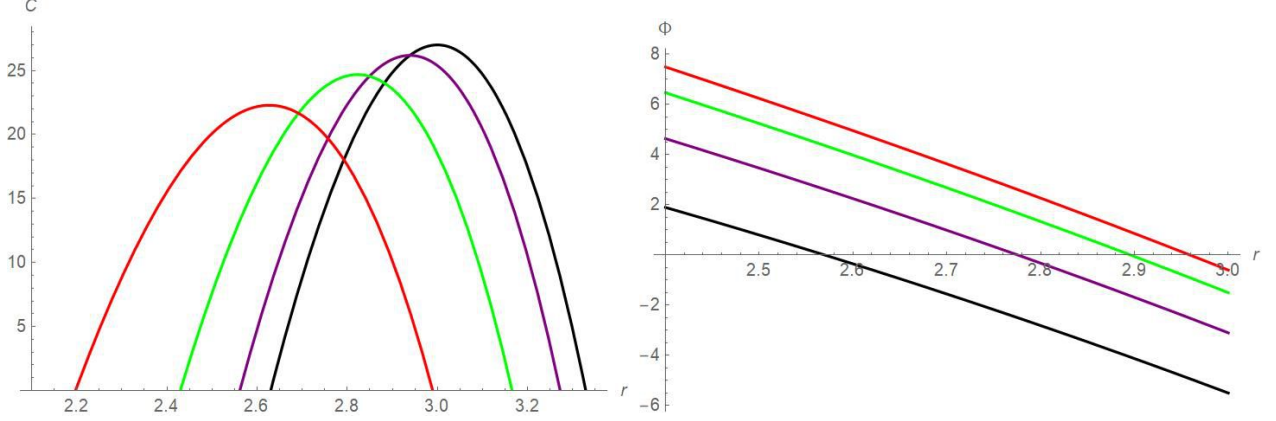$$R(r = r_{SO}) = \left.\frac{dR(r)}{dr}\right|_{r=r_{SO}} = 0. \tag{12}$$

5

FIG. 1: Typical plots of C and Φ as functions of r_{SO} for several values of Q: $Q = 0$ (black), $Q = 0.3M$ (purple), $Q = 0,5M$ (green) dan $Q = 0,7M$ (red).

Solving the two equations simultaneously, we get two conditions:

$$(i) \quad \Phi = \frac{r_{SO}^2 + a^2}{a}, \qquad C = -\frac{r_{SO}^4}{a^2}; \tag{13}$$

$$(ii) \quad \Phi = -\frac{a^2 M + a^2 r_{SO} - 3M r_{SO}^2 + 2Q^2 r_{SO} + r_{SO}^3}{a(r_{SO} - M)},$$

$$C = -\frac{r_{SO}^2 \left[4a^2 \left(Q^2 - M r_{SO} \right) + (r_{SO}(r_{SO} - 3M) + 2Q^2)^2 \right]}{a^2 (r_{SO} - M)^2}. \tag{14}$$

Note that both solutions (13)-(14) satisfy

$$\left. \frac{d^2 R(r)}{dr^2} \right|_{r=r_{SO}} > 0, \tag{15}$$

implying that they are unstable under radial perturbation [21]. The first condition (13) is unphysical [33] since it does not satisfy condition (11). In the second condition (14) C must take a positive sign since $C < 0$ violates the constraint (11).

Qualitatively, the plots of C and Φ look similar to the Kerr case. However, they shift as Q varies, as shown in Fig. 1. As Q increases, the plot of C shifts to the left while its maximum point decreases. Since Carter's constant C represents the angular velocity of the photon in the equatorial direction (as in the Kerr case), for highly-charged black holes the orbits are forced to concentrate on the equatorial plane only.

1. **Analytical Solutions**

The geodesic Eqs. (4)-(8) can be solved analytically. Defining the Mino's parameter λ [26]

$$\frac{d\tau}{d\lambda} \equiv \Sigma \quad \rightarrow \quad \Sigma\frac{dx^\mu}{d\tau} = \frac{dx^\mu}{d\lambda}, \tag{16}$$

the coordinates of (θ, ϕ, t) can be solved in terms of the elliptic integral and the Jacobi elliptic functions [60][61][62]. The Eq. (6) can be cast, by defining $w \equiv u^2$, as

$$\frac{dw}{d\lambda} = \pm 2Y(w), \tag{17}$$

where

$$Y(w)^2 \equiv -a^2 w(w - w_1)(w - w_2), \tag{18}$$

and $w_{1,2}$ are the roots of $Y(w)^2$:

$$w_{1,2} = \frac{a^2 - C - \Phi^2 \pm \sqrt{4a^2 C\left(-C - \Phi^2 + 1\right)^2}}{2a^2}. \tag{19}$$

Choosing the positive sign and taking the initial condition $w(\lambda = 0) = 0$, Eq. (17) can be integrated

$$\lambda = \frac{1}{2}\int_0^w \frac{dw}{Y(w)} = \frac{1}{a\sqrt{w_1 - w_2}}\, F(\Psi, k), \tag{20}$$

where

$$\Psi \equiv \arcsin\sqrt{\frac{w(w_1 - w_2)}{w_1(w - w_2)}}, \quad k \equiv \sqrt{\frac{w_1}{w_1 - w_2}}, \tag{21}$$

and $F(\Psi, k)$ is the *incomplete elliptic integral function of the first kind* [60]. From Eq. (20) it can be seen that λ increases along with w. The one full latitudinal oscillation for λ is

$$\Delta\lambda = \frac{4}{a\sqrt{w_1 - w_2}}K(k), \tag{22}$$

with $K(k)$ is the *complete elliptic integral function of the first kind.*

To obtain the solution for θ, it is necessary to write the inverse of Eq. (20) in the form of the *Jacobi amplitude function*:

$$\Psi = \mathrm{am}(a\sqrt{w_1 - w_2}\lambda, k). \tag{23}$$

by writing the Eq. (23) above in terms of the *elliptic sine sn* function,

$$\sin\Psi = \mathrm{sn}(a\sqrt{w_1 - w_2}\lambda, k), \tag{24}$$

7

the analytical solution of θ can be written as

$$\theta(\lambda) = \arccos\left[\sqrt{-w_2}\, k\, \text{sd}\left(a\sqrt{w_1 - w_2}\lambda, k\right)\right], \tag{25}$$

where $sd(x,y) \equiv sn(x,y)/dn(x,y)$ and $dn(x,y)$ is the so-called *the delta amplitude function* defined as

$$dn(x,y) \equiv \frac{d}{dx}\text{am}(x,y). \tag{26}$$

From Eq. (16), the geodesic equations for ϕ and t can be written

$$\frac{d\phi}{dw} = \frac{1}{2Y(w)}\left[\frac{a(r^2 + a^2 - a\Phi)}{\Delta} - a + \frac{\Phi}{1-w}\right], \tag{27}$$

$$\frac{dt}{dw} = \frac{1}{2Y(w)}\left[\frac{(r^2 + a^2)^2 - (r^2 + a^2)a\Phi}{\Delta} + a\Phi - a^2(1-w).\right] \tag{28}$$

Assuming the initial condition $\phi(w=0) = t(w=0) = 0$, the solutions are

$$\phi(\lambda) = \frac{\Phi}{a(1-w_2)\sqrt{w_1 - w_2}}[F(\Psi, k) - w_2\Pi(\Psi, k^2(1-w_2), k)]$$
$$+ \left[\frac{a(r^2 + a^2 - a\Phi)}{\Delta} - a\right]\lambda, \tag{29}$$

$$t(\lambda) = -\frac{a}{\sqrt{w_1 - w_2}}[(1-w_2)F(\Psi, k) + w_2\Pi(\Psi, k^2, k)]$$
$$+ \left[\frac{(r^2 + a^2)^2 - (r^2 + a^2)a\Phi}{\Delta} + a\Phi\right]\lambda, \tag{30}$$

where $\Pi(\Psi, w_1, k)$ is *the incomplete elliptic integral function of the third kind*. The above two solutions are valid for all values of the λ parameter. When $Q = 0$ the solution reduces to the Teo's [33]. The changes in ϕ and t for a period of $\Delta\lambda$, i.e. one complete latitudinal oscillation, are

$$\Delta\phi = \frac{4}{\sqrt{w_1 - w_2}}\left[\frac{\Phi}{a(1-w_1)}\Pi(-\frac{w_1}{1-w_1}, k) + \left(\frac{r^2 + a^2 - a\Phi}{\Delta} - 1\right)K(k)\right], \tag{31}$$

$$\Delta t = -\frac{4}{\sqrt{w_1 - w_2}}\left\{-a[(1-w_2)K(k) + w_2\Pi(k^2, k)]\right.$$
$$+ \left.\left[\frac{(r^2 + a^2)^2 - (r^2 + a^2)a\Phi}{a\Delta} + \Phi\right]K(k)\right\}. \tag{32}$$

Eq. (31) determines the type of spherical orbits formed around the black hole. When $\Delta\phi$ is positive the orbit is *prograde*, and when it is negative it becomes *retrograde*.

The analytical solutions (25) and (29)-(30) completely specify the photon trajectories. In the following subsections, we shall present and discuss extensively their 3D plots based on the extremality of the black hole.

8

Orbit	Q/M	r_{SO}/M	C/M^2	u_0	$\Delta\phi$
(a)	0	2.671	24.209	1	2.242
(b)	0.6	2.477	21.546	1	2.050
(c)	0.7	2.398	20.5271	1	1.941

TABLE I: Parameters of the SPO around a non-extreme KN for $\Phi = 0$.

2. Non-extreme Kerr-Newman Orbits

The number of KN horizons is parametrized by (II). Here we discuss the non-extremal KN, specifically, we work on the case where

$$a = 0.8\sqrt{M^2 - Q^2}. \tag{33}$$

The constraints (13)-(14) can be used to determine the orbit parameters. Once both angular momenta for the source, a, and the test particle, Φ, are fixed, then the rest of the parameters are completely determined.

In Tables I-II we show orbit parameters for $\Phi = 0, -M$ and several variations of the charge Q. In Fig. 2, we present examples of orbit trajectories for two latitudinal oscillations when $\Phi = 0$ in the $(x - y - z)$ plane, $x - y$, and $x - z$ planes, respectively. Each plot depicts the orbit on an imaginary sphere with a fixed radius r_{SO}. The photons start from the equator and progress northward in each orbit, consistent with the direction of rotation of the black hole itself, which is from west to east. The nine illustrations from Figs. 2 (a), (b), and (c) correspond to cases where $Q = 0$ (Kerr), $Q = 0.6M$, and $Q = 0.7M$, respectively. When $Q = 0.6M$ the orbit veers away from the pole. The presence of spherical photon orbits (SPOs) appears to be hindered by the increasing charge. As depicted in Fig. 2 (c), for $Q = 0.7M$ the photon orbits predominantly concentrate near the equatorial plane.

In Fig. 3 we illustrate three examples of orbits for $\Phi = -M$ in sixteen latitudinal oscillations. Each orbit is plotted on an imaginary sphere with a fixed radius r_{SO} (see Table II). In Fig. 3, plots (a), (b), and (c) correspond to the cases of $Q = 0$ (Kerr), $Q = 0.3M$, and $Q = 0.6M$, respectively. Similar to the previous scenario, an increase in charge causes the orbital trajectory to align more closely with the equatorial plane. Of particular interest is the behavior observed for $Q = 0.6M$: the orbits densely cluster around a segment of solid angle but do not complete a full azimuthal rotation. This phenomenon arises because
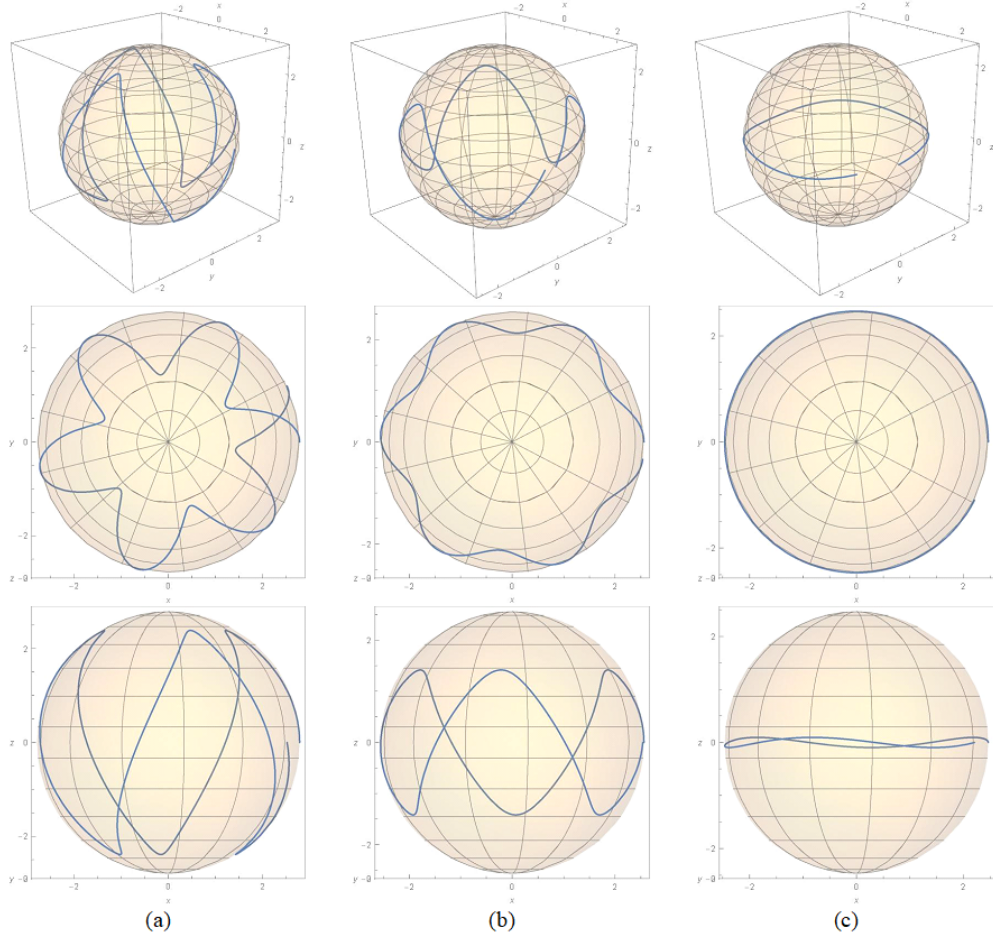
FIG. 2: Two latitudinal oscillations of the photon orbits around the non-extreme KN with $\Phi = 0$ in the $(x - y - z)$ as well as the projective $x - y$ and $x - z$ planes.. The orbit begins from the equator and heads northwards. The direction of the black hole's rotation is from west to east. Figures (a), (b), and (c) are cases with $Q = 0$, $Q = 0.6M$, and $Q = 0.7M$, respectively.

Orbit	Q/M	r_{SO}/M	C/M^2	u_0	$\Delta\phi$
(a)	0	2.882	26.611	0.9821	-0.1922
(b)	0.3	2.833	25.854	0.9815	-0.0299
(c)	0.6	2.669	23.45	0.97967	0.309725

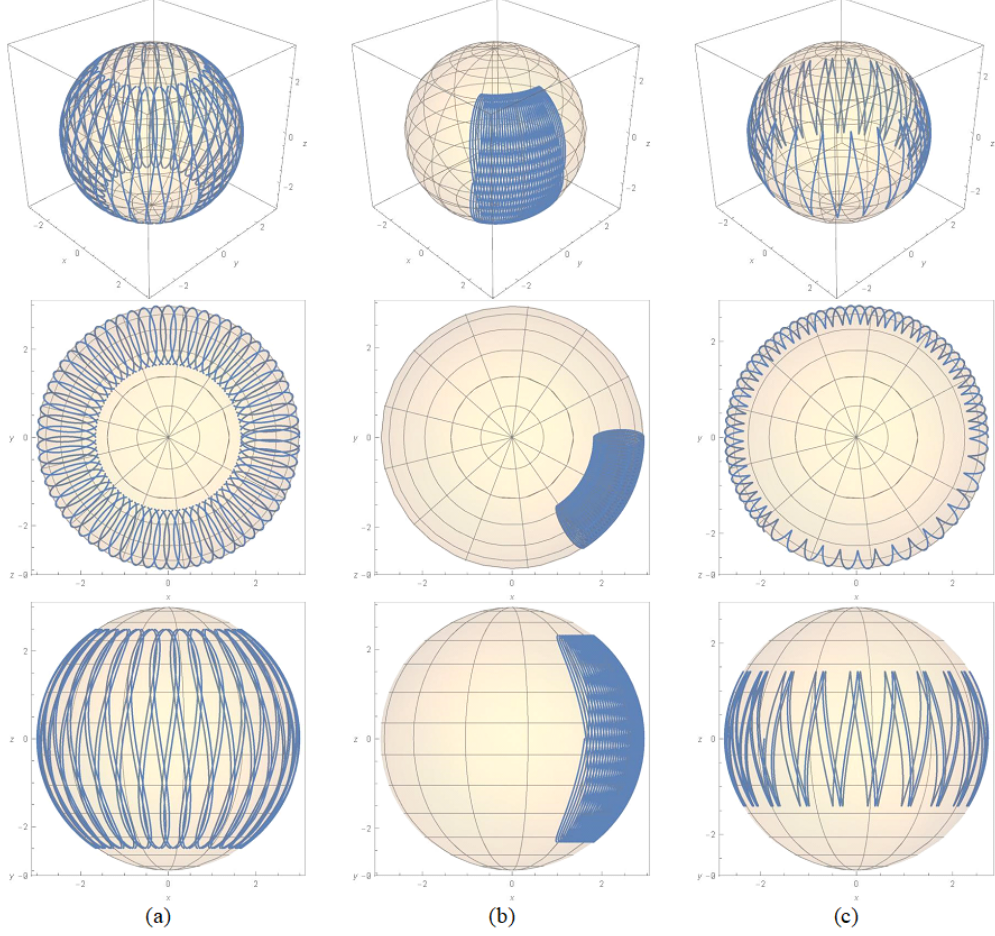TABLE II: Parameters of the SPO around a non-extreme KN for $\Phi = -M$.

FIG. 3: Sixteen latitudinal oscillations of the photon orbits around the non-extreme KN with $\Phi = -M$ in the $(x - y - z)$ as well as the projective $x - y$ and $x - z$ planes. The orbit begins from the equator and heads northwards. The direction of the black hole's rotation is from west to east. Figures (a), (b), and (c) are cases with $Q = 0$, $Q = 0.3M$, and $Q = 0.6M$, respectively.

$Q = 0.6M$ is the transition value between retrograde and prograde motions.

3. Extreme Kerr-Newman Orbit

The extremal KN happens when

$$a = \sqrt{M^2 - Q^2}. \tag{34}$$

In this work, the orbit parameters for extremal KN are shown in Tables III-IV for $\Phi = 0, -M$, respectively. In Fig. 4, we depict three examples of orbits for two latitudinal oscillations

11

Orbit	Q/M	r/M	C/M^2	u_0	$\Delta\phi$
(a)	0	2.414	22.314	1	3.1761
(b)	0.4	2.356	21.372	1	2.473
(c)	0.8	2.166	18.410	1	0.596

TABLE III: Parameters of the spherical photon orbit around extreme Kerr-Newman black hole when $\Phi = 0$.

when the angular momentum of the photon $\Phi = 0$ in the $(x - y - z)$ plane, the $x - y$ and $x - z$ planes respectively. Each plot showcases the orbit on an imaginary sphere with a fixed radius (details regarding the radius and other parameters can be found in Table III). The photons initiate their movement from the equator and progress northward in each orbit, mirroring the direction of rotation of the black hole itself, which is from west to east. The nine illustrations in Figs. 4 (a), (b), and (c) correspond to cases where $Q = 0$, $Q = 0.4M$, and $Q = 0.8M$, respectively. Notably, the orbit depicted in (a) aligns with the one observed in Teo [33], where they touch one another at the poles. However, for $Q = 0.4M$ the orbits, previously tangent to each other, begin to separate. The charge of the black hole begins to change the direction of the photons' orbits at the poles. Upon further increasing the charge to $Q \sim 0.8M$, the two latitudinal oscillations are insufficient to complete an orbit. Additionally, the increased charge concentration renders the orbit more aligned with the equatorial plane, as evidenced in Fig. 4 (c). This trend is attributed to the reduction in the black hole's angular momentum. Furthermore, we investigate the occurrence of a photon boomerang in this extremal case. The boomerang condition,

$$\Delta\phi = \pi, \tag{35}$$

is satisfied when the charge value is small, $Q = 0.02528M$ and $\Phi = 0$. The corresponding plot closely resembles Fig. 4 (a).

In Fig. 5 we illustrate three examples of SPO with $\Phi = -M$ for five latitude oscillations. Each orbit is plotted on an imaginary sphere with a fixed radius whose radius values, as well as other orbital parameters, can be found in Table IV. Figs. 5 (a)-(c) depict the scenarios where $Q = 0$ (Kerr), $Q = 0.5M$, and $Q = 0.6M$, respectively. The presence of charge alters the direction of the photon, and its augmentation prompts the orbit to return to the equatorial plane. Notably, for $Q = 0.6M$ an intriguing phenomenon happens: the photon
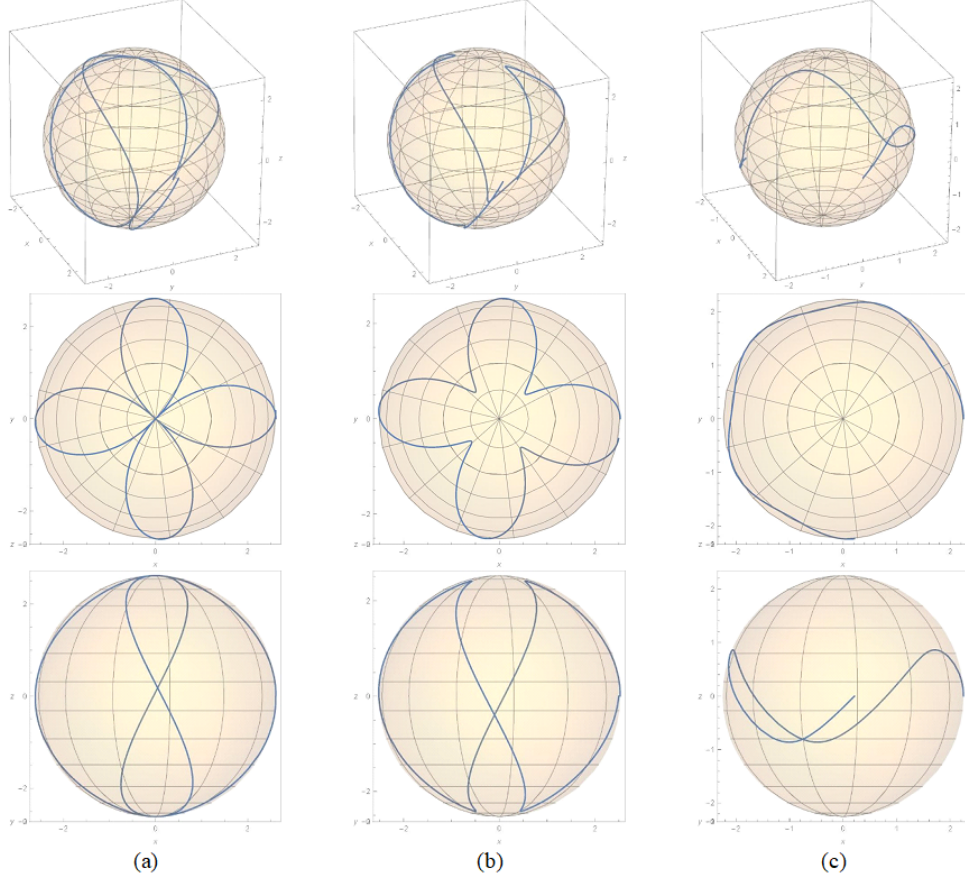
FIG. 4: Two latitudinal oscillations of the photon orbit around the extremal KN with $\Phi = 0$ in the $(x - y - z)$ as well as the projective $x - y$ and $x - z$ planes. The orbit begins from the equator and heads northwards. The direction of the black hole's rotation is from west to east. Figures (a), (b), and (c) are cases with $Q = 0$, $Q = 0.4M$, and $Q = 0.8M$, respectively.

undergoes a twist in its rotation direction about the z axis. Initially retrograde $(Q < 0.6M)$, it abruptly transitions to prograde $(Q \geq 0.6M)$. The charge can effectively steer photons to be in the direction of the black hole's rotation, resulting in a ribbon-shaped orbit, as evidenced in Fig. 5 (c).

B. Spherical Timelike Orbits

The timelike geodesics equations around a Kerr-Newman black hole remain consistent with Eqs. (4)-(8), with $\mu = 1$. Bound and unbound orbits manifest when $E^2 < 1$ and $E^2 > 1$, respectively. Adhering to condition (12), typically yields four solutions. The initial

Orbit	Q/M	r/M	C/M^2	u_0	$\Delta\phi$
(a)	0	2.732	25.85	1	-3.714
(b)	0.5	2.617	23.92	0.9803	-0.3959
(c)	0.6	2.562	23.02	0.9794	0.0303

TABLE IV: Parameters of the spherical photon orbit around Kerr-Newman black hole when $\Phi = -M$.

two solutions are described by:

$$E_{a,b} = \sqrt{\frac{X \pm 2ar_{SO}^2 Y\left(-Mr_{SO} + Q^2\right)\left(a^2 - 2Mr_{SO} + Q^2 + r_{SO}^2\right)}{\Gamma}}, \tag{36}$$

$$\Phi_{a,b} = \frac{ar_{SO}^2 Y\left(Mr_{SO} - Q^2\right)\left[a^2 + r_{SO}(r_{SO} - 2M) + Q^2\right] + \alpha}{\beta} E_{a,b},$$

where

$$X \equiv r_{SO}^2 \left\{ -2a^4\mathcal{C}\left(Q^2 - Mr\right) - a^2 s + r_{SO}^2\left[r_{SO}(r_{SO} - 3M) + 2Q^2\right]\left[r(r_{SO} - 2M) + Q^2\right]^2 \right\}, \tag{37}$$

$$Y \equiv \sqrt{a^2\mathcal{C}^2 + r_{SO}^2\left[3\mathcal{C}Mr_{SO} - r_{SO}^2\left(\mathcal{C} + Q^2\right) - 2\mathcal{C}Q^2 + Mr_{SO}^3\right]}, \tag{38}$$

$$\Gamma = r_{SO}^6\{4a^2(Q^2 - Mr_{SO}) + [2Q^2 + r_{SO}(-3M + r_{SO})]^2\}. \tag{39}$$

$$s \equiv \mathcal{C}\left[r_{SO}^2\left(5M^2 - 4Mr_{SO} + r_{SO}^2\right) + 2Q^2 r_{SO}(r_{SO} - 3M) + 2Q^4\right]$$
$$+ r_{SO}^2\left(Mr - Q^2\right)\left[r_{SO}(3r_{SO} - 5M) + 2Q^2\right], \tag{40}$$

$$\alpha \equiv a^2 r_{SO}\left(Q^2 - Mr_{SO}\right)\left[-Mr_{SO}^2\left(a^2 + \mathcal{C} + 4Q^2\right) + a^2\mathcal{C}M + Q^2 r_{SO}\left(a^2 + \mathcal{C} + Q^2\right)\right]$$
$$+ \left[2r_{SO}^3\left(2M^2 + Q^2\right) - 3Mr_{SO}^4\right]a^2 r_{SO}\left(Q^2 - Mr_{SO}\right), \tag{41}$$

$$\beta \equiv a\, r_{SO}\left(Q^2 - Mr_{SO}\right)\left\{a^2\left[\mathcal{C}(M - r_{SO}) + r_{SO}\left(Q^2 - Mr_{SO}\right)\right]\right.$$
$$\left. + r_{SO}\left[r_{SO}(r_{SO} - 2M) + Q^2\right]^2 \right\}. \tag{42}$$

The third and fourth solutions are related to the first two as the following

$$(E_{c,d}, \Phi_{c,d}) = -(E_{a,b}, \Phi_{a,b}), \tag{43}$$

just like the Kerr case [34]. The first two are, however, the only physical solution: $(E_{a,b}, \Phi_{a,b})$.
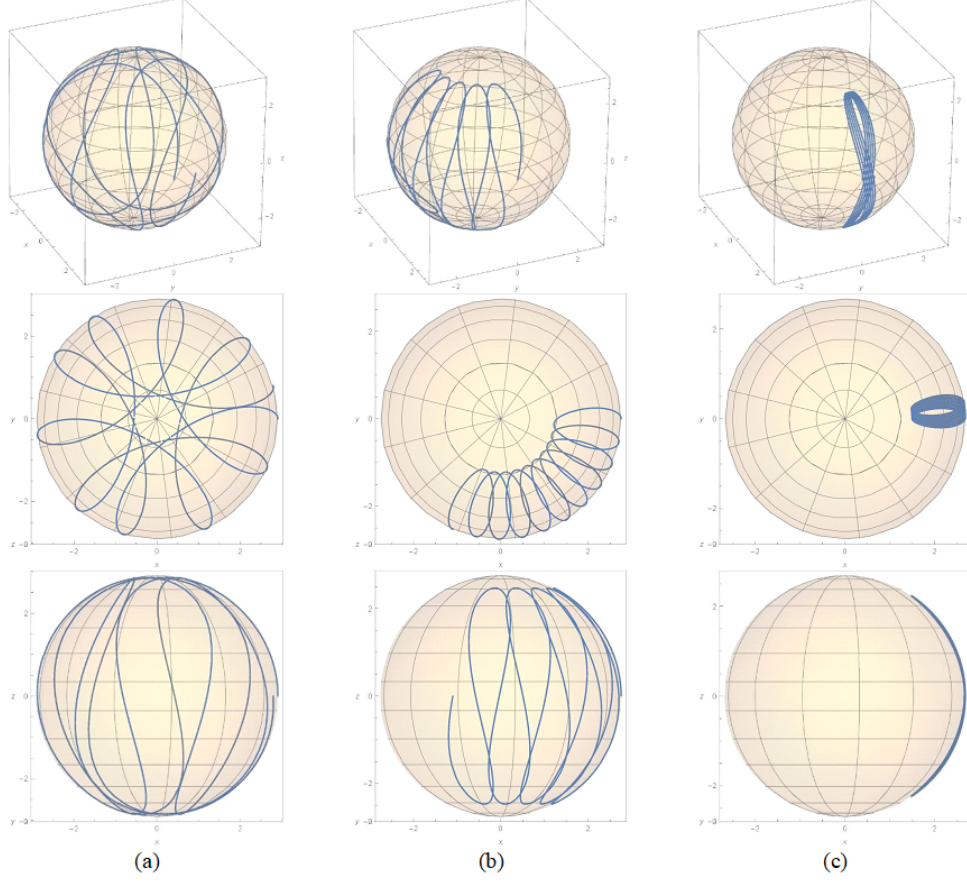
FIG. 5: Five latitudinal oscillations of the photon orbits around extremal KN with $\Phi = -M$ in the $(x - y - z)$ as well as the projective $x - y$ and $x - z$ planes. Figures (a), (b), and (c) are cases with $Q = 0$, $Q = 0.5M$, and $Q = 0.6M$ respectively.

1. Analytical Solutions

The roots of $\Theta(u) = 0$ (Eq. (8)) with $w \equiv u^2$ can be written as

$$w_{1,2} = \frac{\left[a^2\left(1 - E^2\right) + \mathcal{C} + \Phi^2 \mp \sqrt{\left[a^2\left(1 - E^2\right) + \mathcal{C} + \Phi^2\right]^2 - 4a^2\mathcal{C}\left(1 - E^2\right)} \right]}{2\left(1 - E^2\right)}. \tag{44}$$

The ranges of $w_{1,2}$ depend on the sign of $E^2 < 1$ or $E^2 > 1$, and the sign of C. For bound orbit we consider $E^2 < 1$ and $0 \leq w \leq w_1 \leq 1 < w_2$. The exact solutions for (θ, ϕ, t) are

$$\theta(\lambda) = \arccos\left(\sqrt{w_1}\, \text{sn}[a\sqrt{(1-E^2)\, w_2}\, \lambda, k]\right), \tag{45}$$

$$\phi(\lambda) = \frac{\Phi}{a\sqrt{(1-E^2)\, w_2}}\Pi(\Psi, w_1, k) + \frac{aP - a\Delta F}{\Delta}\lambda, \tag{46}$$

$$t(\lambda) = -\frac{aE}{\sqrt{(1-E^2)w_2}}[(1-w_2)F(\Psi, k) + w_2 E(\Psi, k)]$$

$$+ \left[\frac{(r^2+a^2)^2 - (r^2+a^2)a\Phi}{\Delta} + a\Phi\right]\lambda, \tag{47}$$

where $E(\psi, k)$ is *the incomplete elliptic integral of the second kind*, and

$$\Psi \equiv \text{am}(a\sqrt{(1-E^2)\, w_2}\, \lambda, k), \quad k \equiv \sqrt{\frac{w_1}{w_2}}. \tag{48}$$

θ is a periodic function of λ, with period

$$\Delta\lambda = \frac{4}{a\sqrt{(1-E^2)\, w_2}}K(k). \tag{49}$$

The change in ϕ and t for one period are

$$\Delta\phi = \frac{4}{a\sqrt{(1-E^2)\, w_2}}\left[\frac{\Phi}{a}\Pi(w_1, k) + \frac{a(P - E\Delta)}{\Delta}K(k)\right], \tag{50}$$

$$\Delta t = -\frac{4}{a\sqrt{(1-E^2)\, w_2}}\left\{-a[(1-w_2)K(k) + w_2 E(k)]\right.$$

$$+ \left.\left[\frac{(r^2+a^2)^2 - (r^2+a^2)a\Phi}{a\Delta} + \Phi\right]K(k)\right\}. \tag{51}$$

For $E^2 > 1$ the orbits become unbound, and the range of w is $w_2 < 0 \leq w \leq w_1 \leq 1$. The exact solutions for (θ, ϕ, t) are similar to the Eqs. (45)-(47), only that the elliptic functions have imaginary modulus [34]. The case for $E^2 = 1$ is known as the *marginally bound orbits [63]*.

2. Selected Orbit

The analytical solutions described by Eqs. (45)-(47) offer insight into the behavior of STOs. We will focus on plotting the case of extreme Kerr-Newman (KN) only, as the non-extreme scenario exhibits similar qualitative behavior. In Fig. 6, we present three examples of orbits corresponding to $\Phi = 0$. Each plot depicts the orbit on an imaginary sphere with

Orbit	Q/M	r_{SO}/M	E	u_0	$\Delta\phi$
(a)	0	10	0.9559	1	0.4869
(b)	0.45	10.39	0.9570	0.8930	0.4624
(c)	0.999	11.74	0.9606	0.045	0.3915

TABLE V: Parameters for STO around extremal KN with $\Phi = 0$ and $C = 14.1M$.

Orbit	Q/M	r_{SO}/M	E	u_0	$\Delta\phi$
(a)	0	7	0.9500	0.9313	-46.4684
(b)	0.45	8.5361	0.9526	0.8317	-14.3344
(c)	0.999	11.35	0.9595	0.0416	-50.765

TABLE VI: STO parameters around the extremal Kerr-Newman black hole with $\Phi = -1.350M$ and $C = 12M$.

a fixed radius (its value is provided in Table V). The particle initiates its movement from the equator and progresses northward in each orbit, in alignment with the rotation direction of the black hole itself, which is from west to east. As the charge increases, the orbits progressively concentrate more around the equator. When $Q = 0.999M$ (approaching the limit $Q \to M$) the orbit effectively becomes equatorial.

In Fig. 7 we depict STOs for $\Phi = -1.350M$, with the radii and other orbit parameters detailed in TableVI. These orbits are plotted for $Q = 0$, $Q = 0.45M$, and $Q = 0.999M$, respectively. As the charge Q increases, it not only alters the orbital direction of the test particle but also confines the orbit closer to the equatorial plane. However, unlike photon orbits, we observe that in the timelike case, there is no transition from retrograde to prograde motion with increasing charge.

3. Innermost Stable Spherical Orbits

From Eq.(5), it is evident that the function $R(r)$ in (8) serves as the effective radial potential, $V_{eff}(r) \equiv -R(r)$. Analogous to static cases, extrema typically exist for each specific choice of parameters, representing stable or unstable spherical orbits. At certain critical parameter values, these extrema merge. In the context of equatorial motion, this
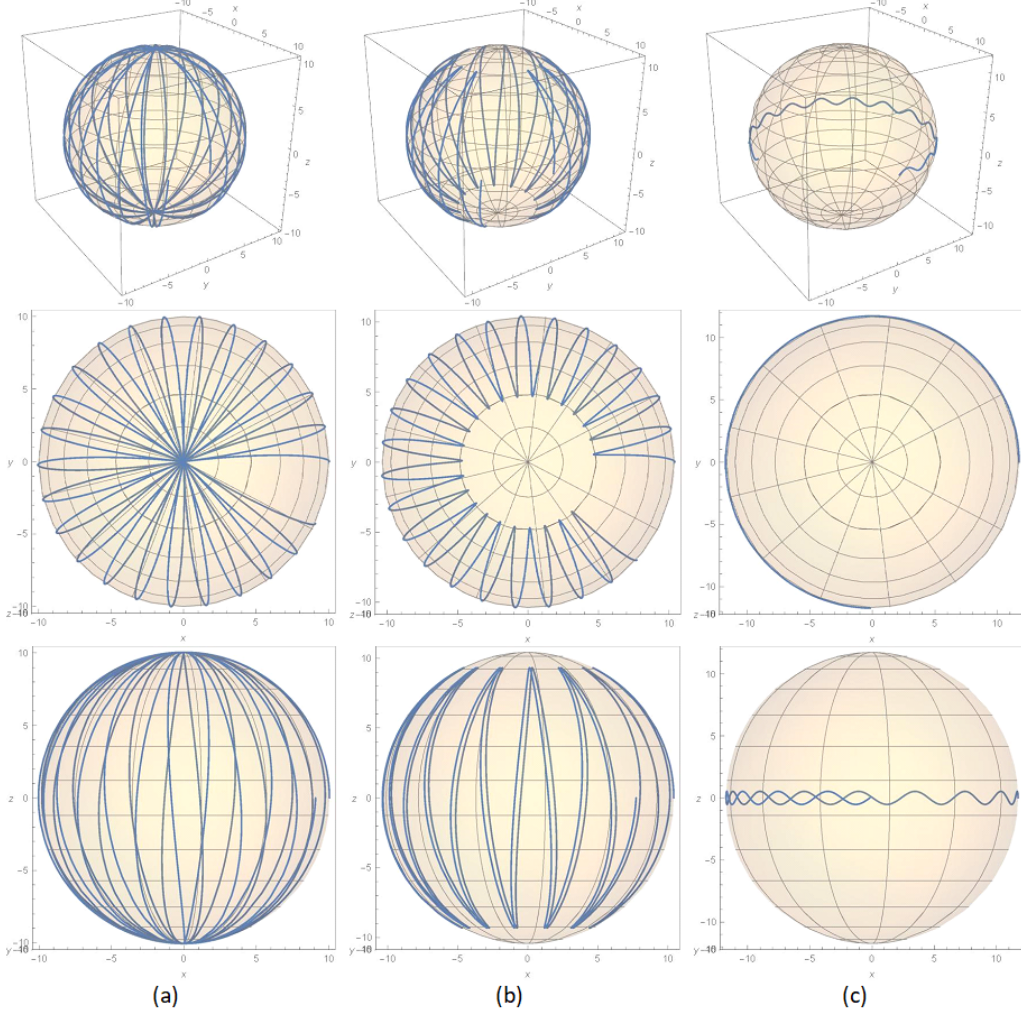
FIG. 6: Spherical timelike orbits of extremal KN with $\Phi = 0$ and $C = 14.1M$ in the $(x - y - z)$ as well as the projective $x - y$ and $x - z$ planes. The orbit begins from the equator and heads northwards. The direction of the black hole's rotation is from west to east. Figures (a), (b), and (c) are cases with $Q = 0$, $Q = 0.45M$, and $Q = 0.999M$, respectively.

phenomenon is referred to as the "innermost stable circular orbit" (ISCO), while for spherical motion, it is termed the "innermost stable spherical orbit" (ISSO) [64]. The ISSO is defined as:

$$V_{eff}(r)\bigg|_{r=r_{ISSO}} = \frac{dV_{eff}(r)}{dr}\bigg|_{r=r_{ISSO}} = \frac{d^2V_{eff}(r)}{dr^2}\bigg|_{r=r_{ISSO}} = 0. \tag{52}$$

18

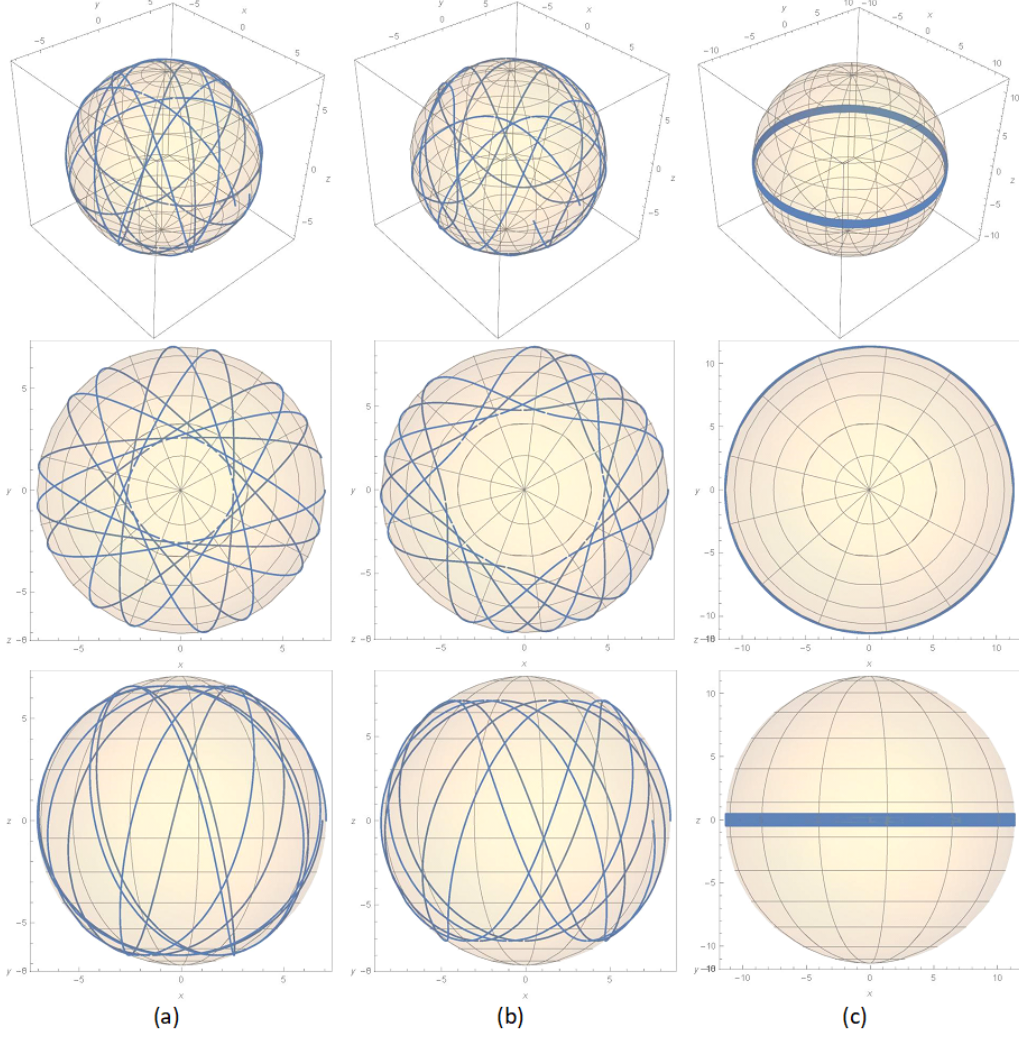FIG. 7: Spherical orbit for extremal KN with $\Phi = -1350M$ and $C = 12M$ in $(x-y-z)$ plane, the projective $x-y$ and $x-z$ plane. The orbit begins from the equator and heads northwards. The direction of the black hole's rotation is from west to east. Label (a), (b), and (c) are cases when the charged value is $Q = 0$, $Q = 0.45M$, and $Q = 0.999M$ respectively.

This condition, supplemented with Eq. (36), yields

$$\frac{-\gamma + \delta + f + 6Mr\sqrt{\sigma} - 8Q^2\sqrt{\sigma}}{rT\left(Mr - Q^2\right)} = 0, \tag{53}$$

$$\frac{V\left(\gamma + \delta - f + 6Mr\sqrt{\sigma} - 8Q^2\sqrt{\sigma}\right)}{T} = 0, \tag{54}$$

for the ($\pm$) conditions, respectively. Here,

$$
\begin{aligned}
\delta &\equiv S\left(8r_{ISSO}^2\left(C\left(3M^2+Q^2\right)-Q^4\right)-26CMQ^2r_{ISSO}+8CQ^4+U\right), \\
\gamma &\equiv 2a^4Cr_{ISSO}^2\left(4Q^2-5Mr_{ISSO}\right)\left(Q^2-Mr_{ISSO}\right), \\
V &= ar_{ISSO}\left(a^2\eta+r_{ISSO}\left(r_{ISSO}(r_{ISSO}-2M)+Q^2\right)^2\right), \\
T &\equiv 4a^2\left(Q^2-Mr_{ISSO}\right)+\left(r_{ISSO}(r_{ISSO}-3M)+2Q^2\right)^2, \\
f &\equiv \xi r_{ISSO}^4\left(Q^2-Mr_{ISSO}\right)\left(r_{ISSO}(r_{ISSO}-3M)+2Q^2\right), \\
\sigma &\equiv S^2\left(a^2+r_{ISSO}(r_{ISSO}-2M)+Q^2\right)^2\zeta, \\
S &\equiv a^2r_{ISSO}^2\left(Q^2-Mr_{ISSO}\right), \\
U &\equiv r_{ISSO}^4\left(4C-7M^2+4Q^2\right)+2Mr_{ISSO}^3\left(7Q^2-9C\right)-3Mr_{ISSO}^5, \\
\xi &\equiv \left(-9MQ^2r_{ISSO}+Mr_{ISSO}^2(6M-r_{ISSO})+4Q^4\right), \\
\zeta &\equiv \left(a^2C^2+r_{ISSO}^2\left(3CMr_{ISSO}-r_{ISSO}^2\left(C+Q^2\right)-2CQ^2+Mr_{ISSO}^3\right)\right), \\
\eta &\equiv C(M-r_{ISSO})+r_{ISSO}\left(Q^2-Mr_{ISSO}\right).
\end{aligned}
\tag{55}
$$

We solve these equations to derive r_{ISSO} as a function of Carter constant. The resulting plot is depicted in Fig. 8, aligning with the findings of Wang, Lee, and Lin [32]. For each fixed value of a and Q, two branches of observable $r_{ISSO}(C)$ exist outside the horizons. The upper branch originates at $r_{ISSO}/M \sim 8.13$, while the lower branch begins at $r_{ISSO}/M \sim 3.39$. These branches merge at a critical value $r_{ISSO}/M \sim 6$, corresponding to $C_{crit}/M^2 \sim 12.23$, beyond which no r_{ISSO} exists. The associated ISSO trajectory is illustrated in Fig. 9, with $r_{ISSO} = 1.00085M$. While the trajectory may initially appear dense around the equator, it is important to note that the figure only depicts one-thirtieth of a complete latitudinal oscillation. A simulation of a full latitudinal oscillation reveals that the orbit fills the entire solid angle.

III. SPHERICAL ORBITS AROUND REGULAR BLACK HOLE

In 1968, Bardeen introduced a regular metric that lacked a physical singularity, exhibiting regularity in both the metric and all invariants as $r \to 0$ [49]. However, Bardeen did not explicitly detail the method used to derive this solution in his original work. Later, Ayon-Beato and Garcia provided an explanation, demonstrating that such a solution can
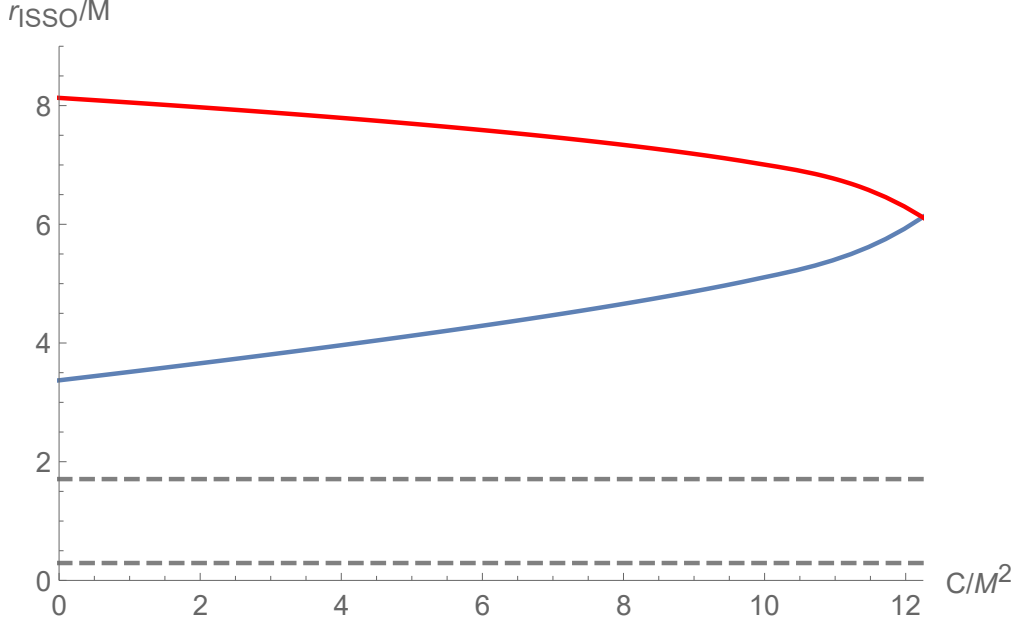
FIG. 8: Plot of r_{isso} as a function of C for $a = 0.7M$ and $Q = 0.1M$. The dashed lines are the corresponding horizons. The blue (red) lines are the negative (positive) roots of Eq. (53) (Eq. (54)), respectively.

be sourced by a nonlinear electrodynamics (NLED) charge [50, 51]. Since then, numerous proposals have emerged regarding nonsingular black holes coupled with NLED. Balart and Vagenas [65], followed by Culetu [66], employed a distribution function inspired by the shape of the probability density function to regularize the static metric. The first to extend this regularization approach to the case of a rotating metric in Boyer-Lindquist coordinates was Ghosh [55], who derived a class of three-parameter axisymmetric metrics:

$$ds^2 = -\left(1 - \frac{2m(r)r}{\Sigma}\right) dt^2 - \frac{4am(r)r}{\Sigma} \sin^2\theta dt \ d\phi + \Sigma\left(\frac{dr^2}{\Delta} + d\theta^2\right) + \frac{\mathcal{A}}{\Sigma}\sin^2\theta d\phi^2,$$

$$\tag{56}$$

where

$$
\begin{aligned}
m(r) &\equiv Me^{-k/r}, \\
\Sigma &\equiv r^2 + a^2\cos^2\theta, \\
\Delta &\equiv r^2 + a^2 - 2m(r)r, \\
\mathcal{A} &\equiv \left(r^2 + a^2\right)^2 - \Delta a^2\sin^2\theta.
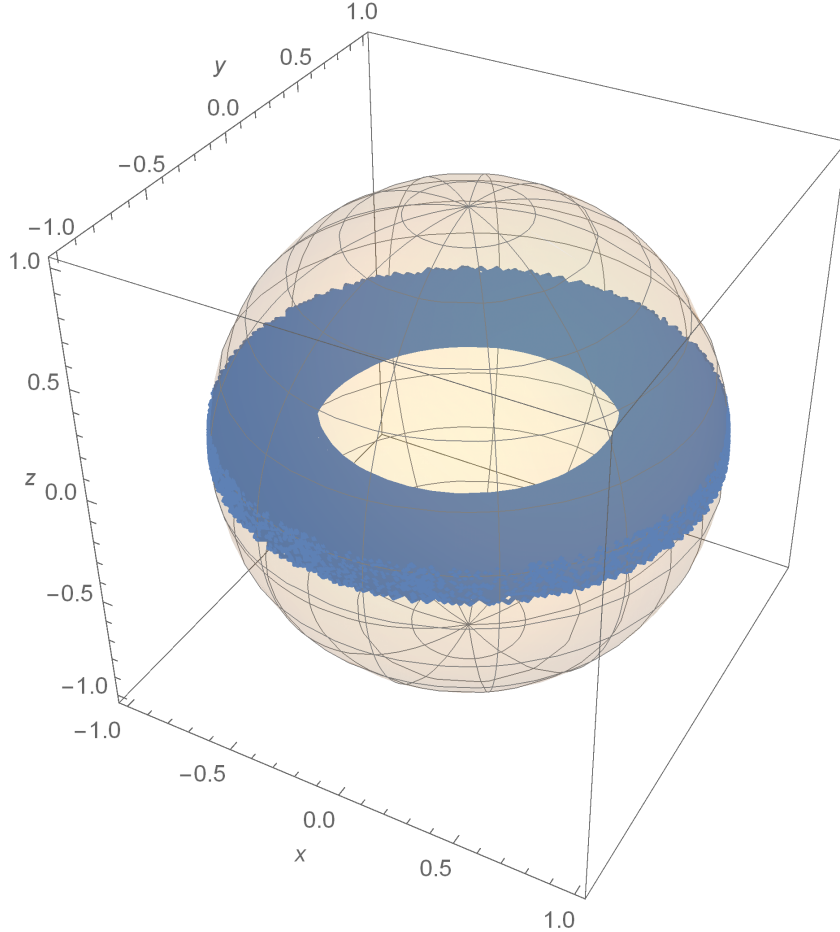\end{aligned}
\tag{57}
$$

21

FIG. 9: ISSO in one-thirtieth second latitude oscillation when $Q = 0.45M$ and $\Phi = 0.192M$ for the extremal KN, having the same energy as in Table VI (b). The corresponding radius is $r_{ISSO} = 1.00085M$. The plot will fill the spherical coordinate as it reaches one latitudinal oscillation.

The metric depends on the mass M, the angular momentum a, and a new parameter k which controls its regularity. The range of a is between $0 < a^2 \leq M^2$, where the upper bound is related to the extreme condition or even "naked" (depending on the value of k) and the lower bound is Schwarzschild black hole (for $k = 0$). The event horizons $r_\pm$ satisfy

$$r_\pm^2 + a^2 - 2m(r_\pm) = 0. \tag{58}$$

Here the radii $r_\pm$ can only be obtained numerically.

Ghosh obtained the solution (56) by transforming the non-singular static black holes [65, 66] to the rotating solutions via the Newman-Janis algorithm [67]. At the core ($r \to 0$) all the invariants of this metric are regular everywhere. Specifically, the *Kretschmann* scalar

22

(K) approaches zero there, $K(r \to 0) \to 0$. For $k = 0$ the metric reduces to Kerr (when $a \neq 0$) or Schwarzschild (when $a = 0$). In the non-rotating limit $(a \to 0)$ the metric reduces to the regular spherically-symmetric black hole [65, 66]

$$ds^2 = -\left(1 - \frac{2Me^{-k/r}}{r}\right)dt^2 + \left(1 - \frac{2Me^{-k/r}}{r}\right)^{-1}dr^2 + d\Omega_2^2. \tag{59}$$

Interestingly, the spacetime structure at the core is (as long as $r \gg k$) Minkowski/RS-like,

$$\left(1 - \frac{2Me^{-k/r}}{r}\right) \approx 1 - \frac{2M}{r} + \frac{2Mk}{r^2} + \mathcal{O}\left(r^{-3}\right), \tag{60}$$

rather than de Sitter-like, as in the Bardeen case [49, 51, 68].

A. Spherical Photon Orbits

1. Equation of Motion

The four geodesic equations of photons in regular rotating space-time are

$$\Sigma\Delta\dot{t} = \mathcal{A}E - 2am(r)rL_z, \tag{61}$$

$$\Sigma\Delta\dot{\phi} = 2am(r)rE + (\Sigma - 2m(r)r)\frac{L_z}{\sin^2\theta}, \tag{62}$$

$$\Sigma^2\dot{\theta} = \mathcal{C} - \left[\frac{L_z}{\sin^2\theta} - E^2a^2\right]\cos^2\theta, \tag{63}$$

$$\Sigma^2\dot{r} = E^2r^4 + \left(E^2a^2 - L_z^2 - \mathcal{C}\right)r^2 + 2m(r)r\left[(aE - L_z)^2 + \mathcal{C}\right] - a^2\mathcal{C}. \tag{64}$$

The notation of E, L_z, and $\mathcal{C}$ are the same three constants of motion-defined previously.

The geodesic equation of θ has a similar form with Kerr. Setting $u = \cos\theta$, Eq. (63) can be rewritten as

$$\left(\frac{\Sigma}{E}\right)^2 \dot{u}^2 = C - \left(C + \Phi^2 - a^2\right)u^2 - a^2u^4, \tag{65}$$

where the new parameters are

$$\Phi \equiv \frac{L_z}{E}, \quad C \equiv \frac{\mathcal{C}}{E}. \tag{66}$$

The physical requirement is also similar to Kerr's black hole. When $C > 0$, the positive root of (65) is

$$u_0^2 = \frac{(a^2 - C - \Phi^2) + \sqrt{(a^2 - C - \Phi^2)^2 + 4a^2C}}{2a^2}. \tag{67}$$
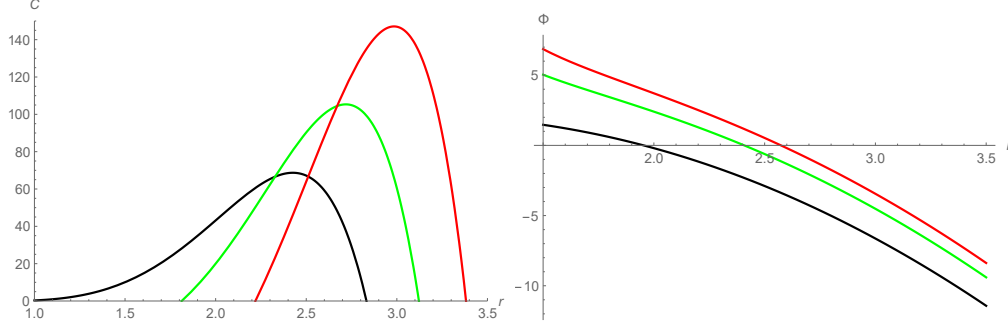
For $C < 0$,

$$a^2 - C - \Phi^2 > 0. \tag{68}$$

23

FIG. 10: Typical plots of C and Φ as functions of r_{SO} for several values of k: $k = 0.1M$ (red), $k = 0.3M$ (green), and $k = 0.5M$ (black).

2. Requirement for the Existence of SPO

Solving the two conditions resulting from Eq. (12) simultaneously we get

$$(i) \quad \Phi = \frac{r_{SO}^2 + a^2}{a}, \quad C = -\frac{r_{SO}^4}{a^2}; \tag{69}$$

$$(ii) \quad \Phi = \frac{a^2 kM + a^2 r_{SO}^2 e^{k/rso} + a^2 M r_{SO} + kM r_{SO}^2 + r_{SO}^4 e^{k/rso} - 3M r_{SO}^3}{a\left(kM - r_{SO}^2 e^{k/rso} + Mr_{SO}\right)},$$

$$C = -\frac{r_{SO}^4 \left\{ 4a^2 M e^{k/rso}(k - r_{SO}) + \left[r_{SO}\left(r_{SO}e^{k/rso} - 3M\right) + kM \right]^2 \right\}}{a^2 \left[r_{SO}\left(M - r_{SO}e^{k/rso}\right) + kM \right]^2}. \tag{70}$$

As in the KN case, both possibilities satisfy condition (15) for all $r_+ < r_{SO}$. Thus, all SPOs here are also unstable. Solution (69) can be ruled out, and so the acceptable one is (70) with $C > 0$ to satisfy condition (68). The behavior of $C(r_{SO})$ and $\Phi(r_{SO})$ for Ghosh BH are depicted in Fig. 10. They look similar to the KN case, Fig. 1, but due to the nature of $m(r)$ the plots are not linear but bent around a small value of r_{SO}.

3. Analytical Solutions

Once again we employ the Mino formalism (16) to solve Eqs. (62)-(64). The geodesic equations for ϕ and t can be written

$$\frac{d\phi}{dw} = \frac{1}{2Y(w)}\left[\frac{2am(r)r - a^2\Phi}{\Delta} + \frac{\Phi}{(1-w)}\right], \tag{71}$$

$$\frac{dt}{dw} = \frac{1}{2Y(w)}\left[\frac{(r^2 + a^2)^2 - 2a\Phi m(r)r}{\Delta} - a^2(1-w),\right] \tag{72}$$

24

where $Y(w)$ is the same as in Eq. (18). Assuming the initial condition $\phi = t = 0$ when $w = 0$, the analytic solution of ϕ and t can be written as

$$\phi(\lambda) = \frac{\Phi}{a(1-w_2)\sqrt{w_1 - w_2}}[F(\Psi, \kappa) - w_2\Pi(\Psi, \kappa^2(1-w_2), \kappa)] \tag{73}$$
$$+ \frac{a}{\Delta}(2m(r)r - a\Phi)\lambda,$$

$$t(\lambda) = -\frac{a}{\sqrt{w_1 - w_2}}[(1-w_2)F(\Psi, \kappa) + w_2\Pi(\Psi, \kappa^2, \kappa)] \tag{74}$$
$$+ \frac{1}{\Delta}\left[(r^2 + a^2)^2 - 2a\Phi m(r)r\right]\lambda,$$

where Ψ and κ are given by Eq. (21). The solution for θ is the same as in Eq. (25).

The changes in ϕ and t for one complete latitudinal oscillation are

$$\Delta\phi = \frac{4}{\sqrt{w_1 - w_2}}\left[\frac{\Phi}{a(1-w_1)}\Pi(-\frac{w_1}{1-w_1}, \kappa) + \frac{2m(r)r - a\Phi}{\Delta}K(\kappa)\right], \tag{75}$$

$$\Delta t = \frac{4}{\sqrt{w_1 - w_2}}[-a((1-w_2)K(\kappa) + w_2\Pi(\kappa^2, \kappa))$$
$$+ \frac{(r^2 + a^2)^2 - 2a\Phi m(r)r}{a\Delta}K(\kappa)]. \tag{76}$$

The equation $\Delta\phi$ determines the orbit direction. Positive $\Delta\phi$ means prograde orbit, while negative one means retrograde orbit.

4. Selected Orbits

Using the analytical solutions (θ, ϕ, t) we will show typical of orbits for non-extreme, extreme, and naked conditions of regular rotating black holes. Unlike the KN case, however, here we have an additional parameter to consider, k, which appears non-linearly in the Eq. (58),

$$\left(\frac{r_\pm}{M}\right)^2 + \left(\frac{a}{M}\right)^2 - \frac{2r_\pm}{M}e^{-Mk/r_\pm} = 0. \tag{77}$$

Consequently, the extremality can be achieved by either adjusting a/M or Mk.

Non-extremal

The non-extremal condition is not compatible with $Mk >> 1$ regime. There exists no parameter a/M that satisfies:

1. $Mk >> 1$,

Orbit	Mk	r_{SO}/M	C/M^2	u_0	$\Delta\phi$
(a)	0	2.892	24.412	0.088	22.436
(b)	0.1	2.743	22.524	0.088	23.698
(c)	0.5	1.996	14.245	0.087	33.482

TABLE VII: SPO Parameters around a non-extremal Ghosh black hole with $\Phi = M$ and $a/M = 0.3$.

Orbit	k	a/M	r_{SO}/M	C/M^2	u_0	$\Delta\phi$
(a)	0	1	2.414	22.314	1	3.1761
(b)	0.1	0.899	2.339	21.124	0.809	3.7483
(c)	0.5	0.472	1.953	15.861	0.222	9.931

TABLE VIII: SPO parameters around an extremal Ghosh black hole with $\Phi = 0$.

2. $r_{SO} > r_+ \neq r_-$, and

3. Eq (70),

simultaneously. For example at $a/M \sim 10^{-6}$ the maximum Mk is ~ 0.73. In this work, we choose $a/M = 0.3$, and the maximum Mk we can have here is $Mk \sim 0.5$. In Fig. 11, we depict three examples of orbits with $\Phi = M$ in the $(x - y - z)$, the $x - y$, and $x - z$ planes, respectively. The radius and other parameter values of the orbit are provided in TableVII. The SPOs appear predominantly equatorial, characterized by minimal latitudinal oscillations with elongated oscillation periods. This observation is consistent with expectations for the slowly rotating black hole regime $(0 < a/M < 1)$.

Extremal Condition

Orbit	k	a/M	r_{SO}/M	C/M^2	u_0	$\Delta\phi$
(a)	0	1	2	16	0.971	10.843
(b)	0.1	0.899	1.946	15.182	0.785	8.417
(c)	0.5	0.472	1.675	11.756	0.214	21.825

TABLE IX: SPO parameters around an extremal regular rotating black hole with $\Phi = M$.

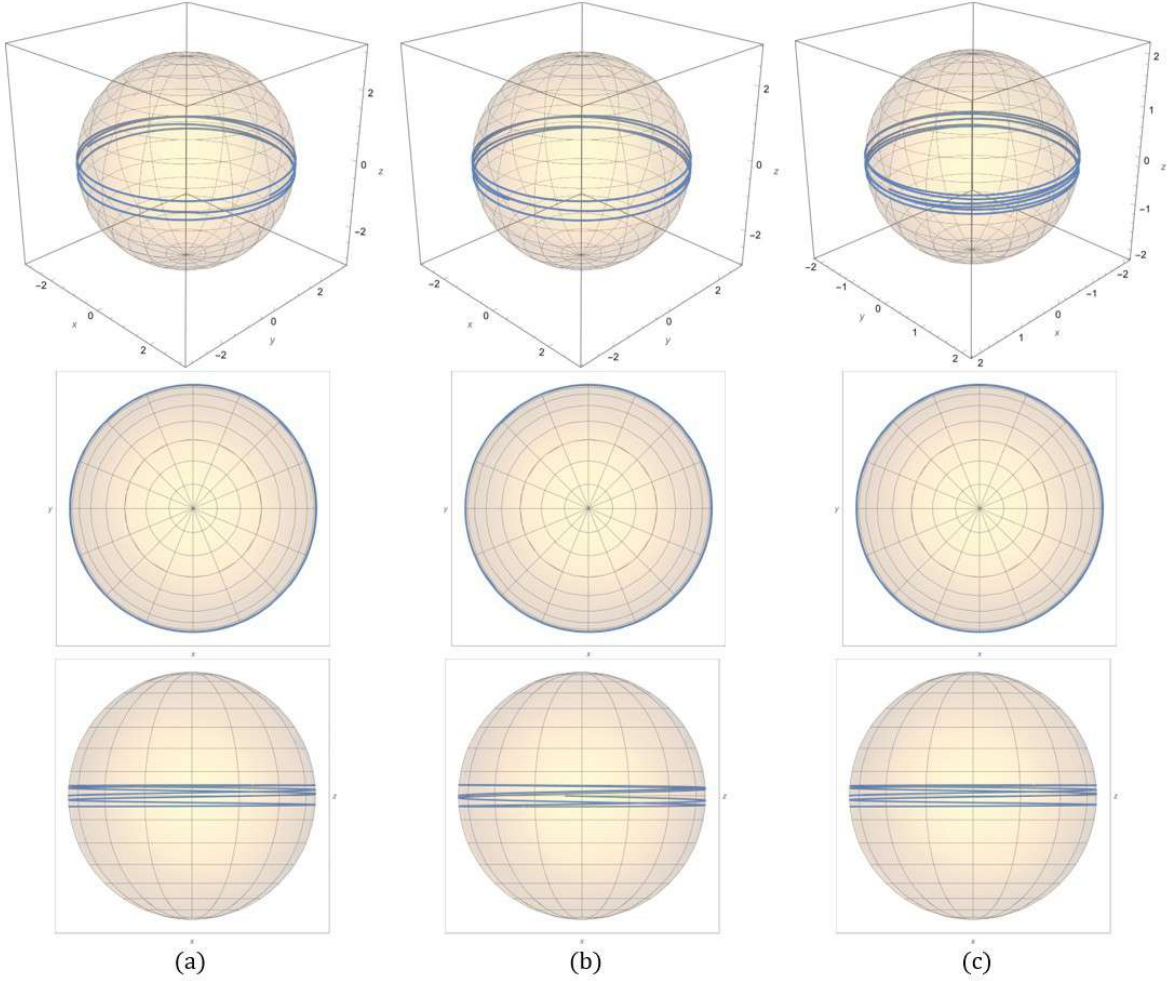FIG. 11: Spherical photon orbits around non-extremal Ghosh black hole with $\Phi = M$ in the $(x-y-z)$ as well as the projective $x-y$ and $x-z$ planes, respectively. The direction of the black hole's rotation is from west to east. Figures (a), (b), and (c) are cases with $Mk = 0$, $Mk = 0.1$, and $Mk = 0.5$, respectively.

The extremal condition turns out to also be incompatible with $Mk >> 1$ regime due to the same reasons as observed in the non-extremal scenario. In this study, we investigate the orbital behavior under the extremal case with $Mk = 0$, 0.1, and 0.5. These cases are illustrated in Figs. 12 (for $\Phi = 0$) and 13 (for $\Phi = M$), respectively, with the corresponding SPO parameters detailed in Tables VIII and IX. For $k = 0$, both SPOs ($\Phi = 0$, M) reduce to the static one previously obtained by Teo in [33]. For each value of fixed Φ it is evident that as Mk increases, the orbits become increasingly confined to the equatorial plane. Moreover, with higher values of Φ, the amplitude of the latitudinal oscillations diminishes, leading to
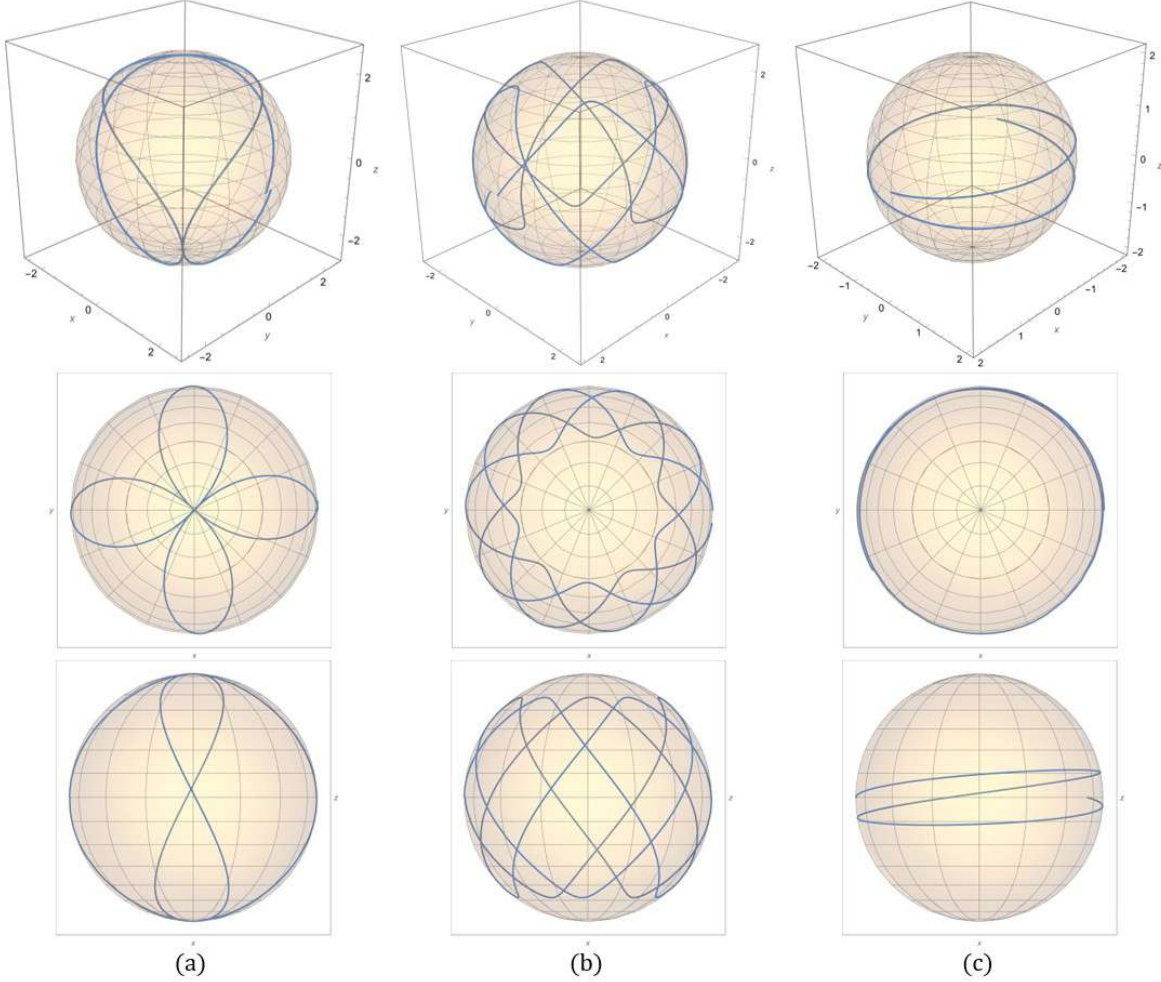
27

FIG. 12: Spherical photon orbits around extremal regular black hole with $\Phi = 0$ in the $(x - y - z)$ as well as the projective $x - y$ and $x - z$ planes. The direction of the black hole's rotation is from west to east. Figures (a), (b), and (c) are cases with $k = 0$, $k = 0.1$, and $k = 0.5$, respectively.

longer oscillation periods.

In the extremal Ghosh black hole case, we also attempted to identify the *photon boomerang*, characterized by the condition where Eq. 75 equals π. Through our numerical investigation, we found only an *approximate* photon boomerang with $k = 0.05$. We label it as "approximate" because the value of $\Phi = 0.07$ is non-zero. This is detailed in Table X, and the corresponding trajectory is depicted in Fig. 14.

No-horizon Spacetime

Certain combinations of a/M, Mk in Eq.(77) can give rise to complex solutions for $r_\pm$. In the context of a conventional black hole, such instances correspond to what is termed a

k	a/M	r_{SO}/M	C/M^2	u_0	$\Delta\phi$
0.05	0.94998	2.402	22.0487	0.902	3.1415

TABLE X: (Approximate) photon boomerang parameters around an extremal regular rotating black hole with $\Phi = -0.07$.
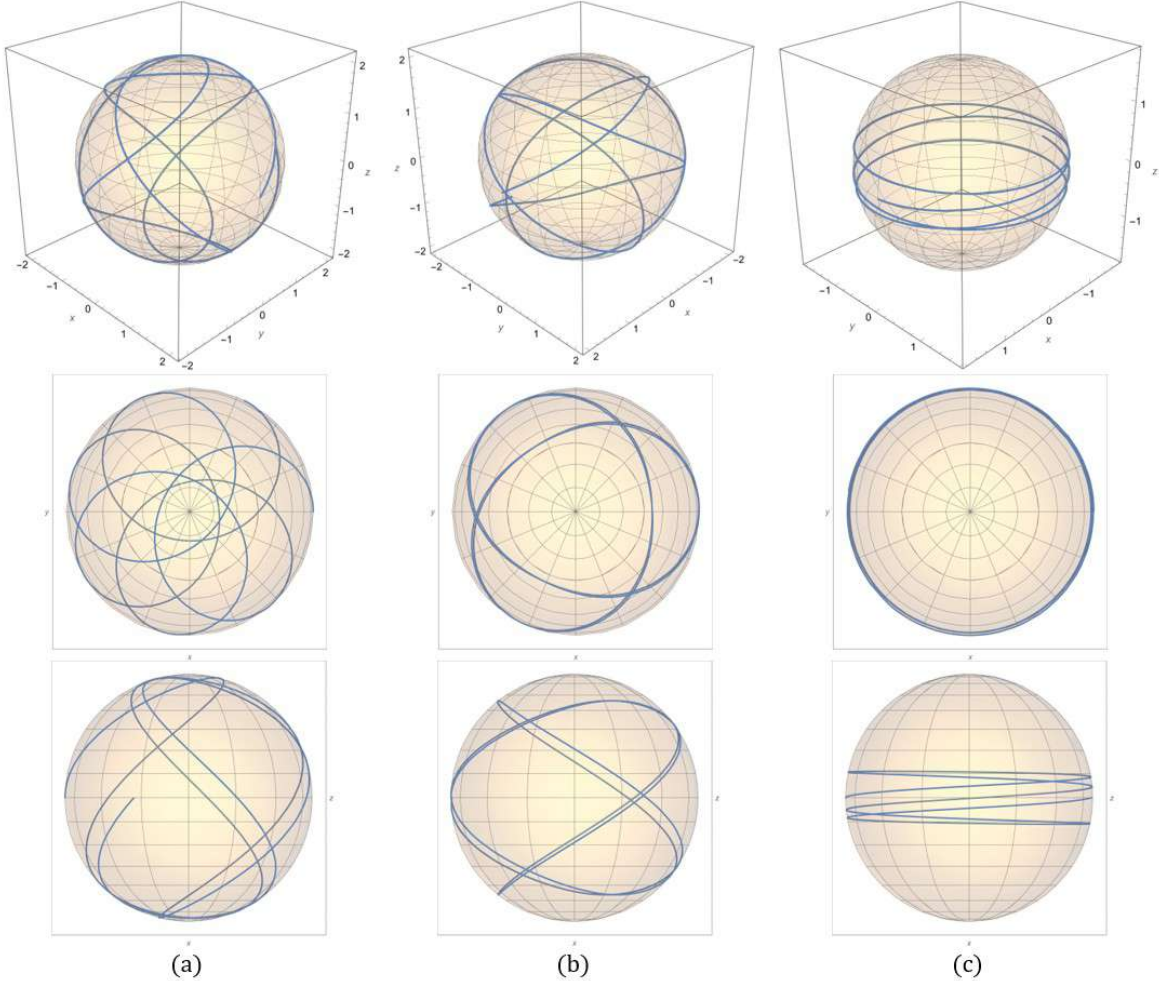

(a)   (b)   (c)

FIG. 13: Spherical photon orbits around extremal Ghosh black hole with $\Phi = M$ in the $(x - y - z)$ as well as the projective $x - y$ and $x - z$ planes. The direction of the black hole's rotation is from west to east. Figures (a), (b), and (c) are cases with $k = 0$, $k = 0.1$, and $k = 0.5$, respectively.

"naked singularity," a phenomenon deemed unstable and unphysical according to the cosmic censorship theorem [69]. However, within the framework of a regular black hole, the concept of singularity vanishes. This scenario is often referred to as "the no-horizon spacetime" in the literature. While discussing trajectories around a naked singularity is nonsensical, the
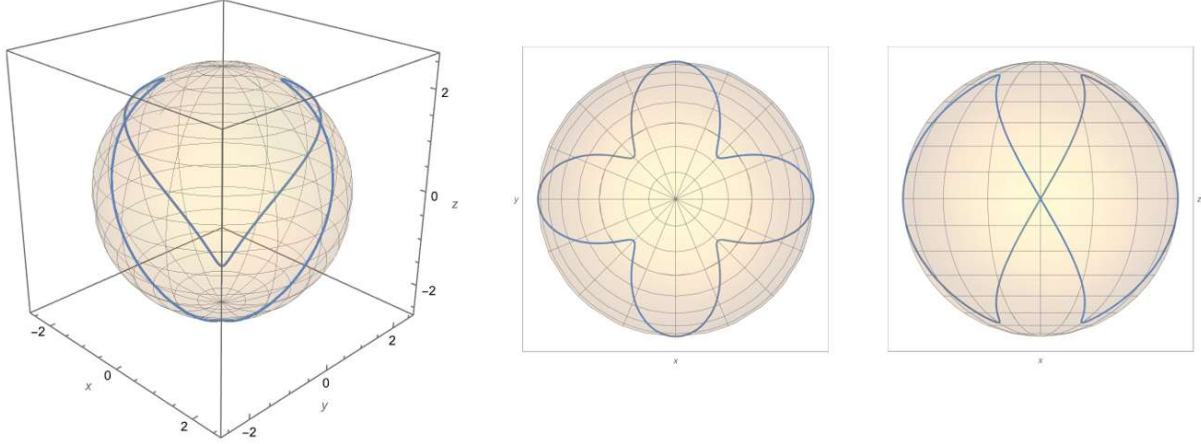
FIG. 14: Photon boomerang around extremal Ghosh black hole with $\Phi = -0.07$ in the $(x - y - z)$ as well as the projective $x - y$ and $x - z$ planes. The direction of black hole's rotation is from west to east.

Orbit	Mk	Φ/M	a/M	r_{SO}/M	C/M^2	u_0	$\Delta\phi$
(a)	0.1	0	1	1.242	24.784	1	11.426
(b)	0.1	-0.55	1	1.178	36.224	0.995	6.291
(c)	0.3	-1.2	1	1.571	20.143	0.967	-0.487
(d)	0.3	-2	1	1.347	26.21	0.933	0.861
(e)	0.5	-2.3	1	1.82	17.377	0.879	-2.04
(f)	0.5	-3.5	1	1.362	21.47	0.802	1.082

TABLE XI: Parameters of the stable SPO around naked regularity.

notion is perfectly acceptable in the case of a regular no-horizon spacetime.

The notion of a regular solution devoid of singularity is not a new concept in GR. Mazur and Mottola [70, 71] discussed an alternative final state of non-singular gravitational collapse by invoking the Bose-Einstein condensate formalism in the interior. The consequence is a horizonless, regular core reminiscent of de Sitter space, which they coined as "*gravastar*". More recently, there has been discourse surrounding the correlation between regular black holes and horizonless ultracompact stars [72–74]. It is pertinent to distinguish that the Ghosh no-horizon solution differs conceptually from the gravastar, as the former features a Minkowski core while the latter exhibits a de Sitter-like core.
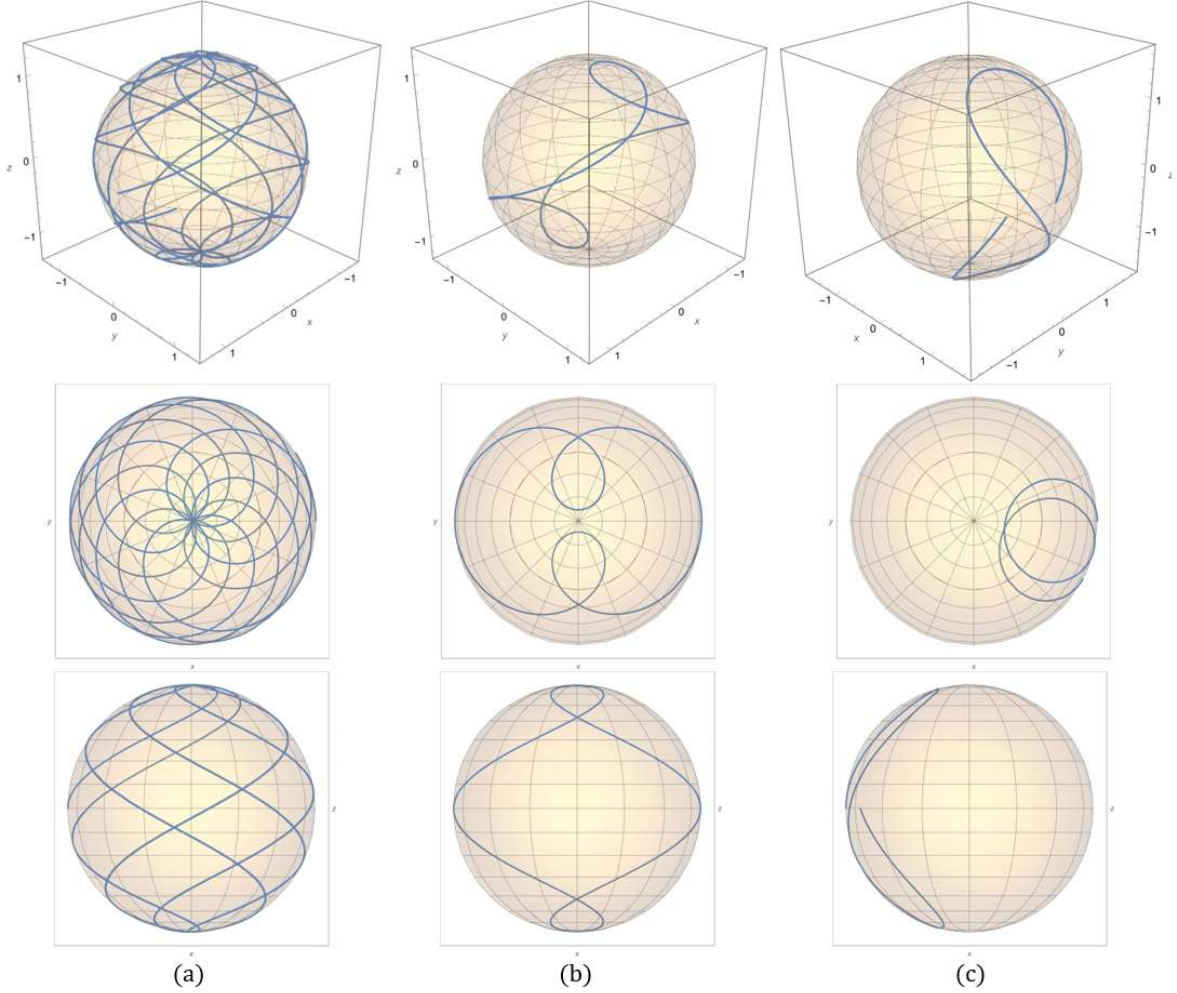
FIG. 15: Spherical photon orbits around no-horizon spacetime in the $(x - y - z)$ as well as the projective $x - y$ and $x - z$ planes. The direction of the black hole's rotation is from west to east. (a) $\Phi = 0$ and $Mk = 0.1$, (b) $\Phi = -0.55M$ and $Mk = 0.1$, (c) $\Phi = -1.2M$ and $Mk = 0.3$.

The absence of a horizon in the geometry opens avenues for stable SPOs (and STOs) by circumventing Eq.(15). Here, we aim to explore the existence of stable spherical orbits around it, adhering to the condition:

$$\frac{d^2 R(r)}{dr^2} < 0. \tag{78}$$

However, our investigation uncovers that conditions (78) and (70) harmonize only when $\Phi \leq 0$. We illustrate orbit trajectories around the no-horizon solution in Figs. 15-16, delineating parameters detailed in Table XI. Each figure represents distinct values of Φ and k, as the stability requirement imposes stringent constraints on them. Given the negative Φ values, the occurrence of the *Lens-Thirring effect* is inevitable. This phenomenon exerts a
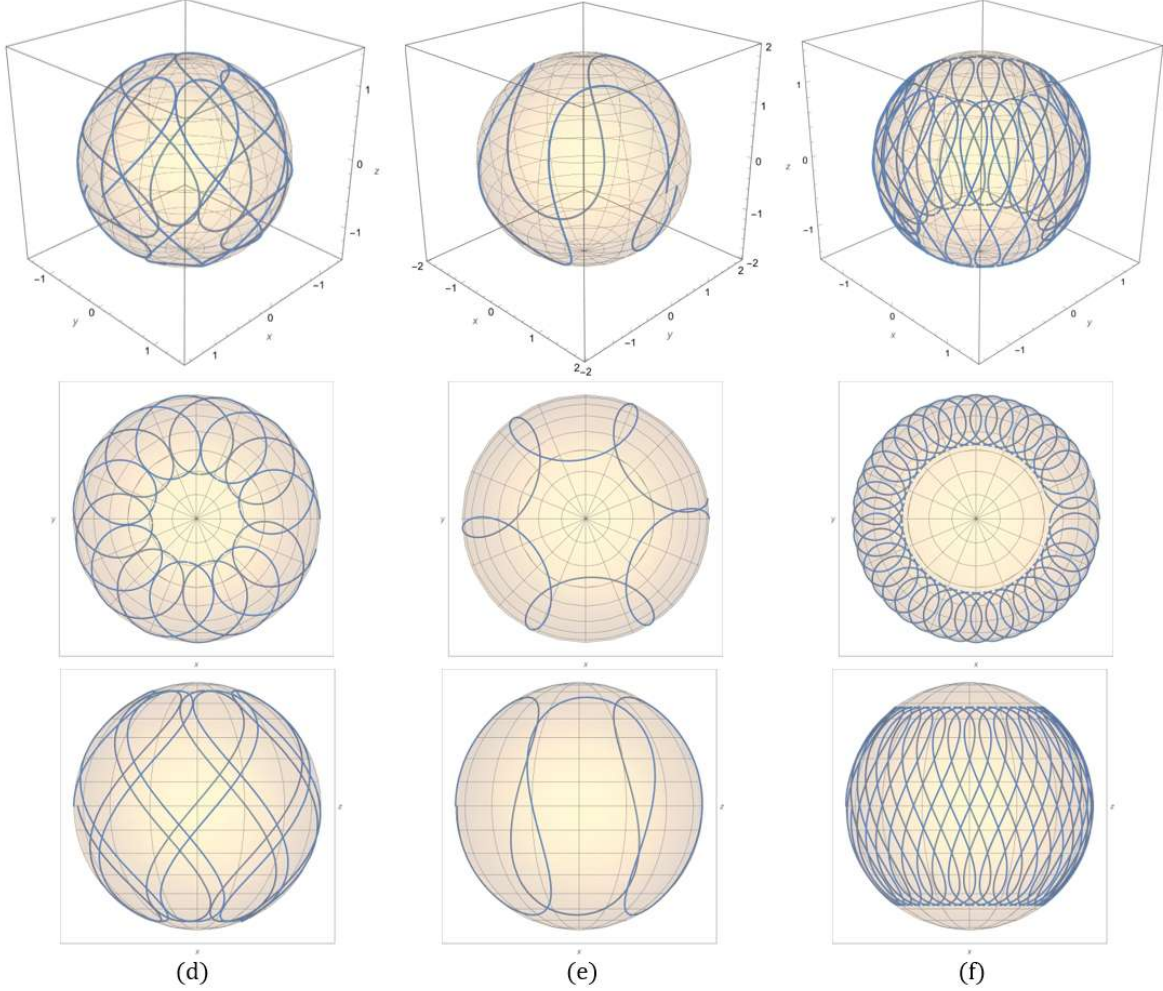
31

FIG. 16: Spherical photon orbits around no-horizon spacetime in the $(x - y - z)$ as well as the projective $x - y$ and $x - z$ planes. The direction of the black hole's rotation is from west to east. (d) $\Phi = -2M$ and $Mk = 0.3$, (e) $\Phi = -2.3M$ and $Mk = 0.5$, (f) $\Phi = -3.5M$ and $Mk = 0.5$.

pronounced influence on orbits near the equator compared to those near the poles. Notably, orbits with negative Φ values maintain a prograde motion around the equator, transitioning to a retrograde direction as they approach the poles. This observation holds particular significance for orbits with $\Phi \sim 0$, as the Lens-Thirring effect possesses the capability to counteract the photon's angular momentum.

B.   Spherical Timelike Orbits

The geodesics equations for an uncharged timelike particle are

$$\Sigma \dot{t} \;=\; -a^2 E\left(1-u^2\right) + \frac{1}{\Delta}\left[E\left(r^2+a^2\right)^2 - 2a\Phi m(r)r\right], \tag{79}$$

$$\Sigma \dot{\phi} \;=\; \frac{\Phi}{1-u^2} + \frac{a}{\Delta}\left(2Em(r)r - a\Phi\right), \tag{80}$$

$$\Sigma \dot{u} \;=\; \pm\sqrt{V\left(u\right)}, \tag{81}$$

$$\Sigma \dot{r} \;=\; \pm\sqrt{R\left(r\right)}, \tag{82}$$

where

$$
\begin{aligned}
R\left(r\right) &\equiv \left(E^2-1\right)r^4 + 2m(r)r^3 + \left[a^2\left(E^2-1\right)-\mathcal{C}-\Phi^2\right]r^2 \\
&\quad + 2m(r)rr\left[(aE-\Phi)^2+\mathcal{C}\right]re^{-k/r} - a^2\mathcal{C}, \\
V\left(u\right) &\equiv a\left(1-E^2\right)u^4 - \left[a^2\left(1-E^2\right)+\mathcal{C}+\Phi^2\right] + \mathcal{C}.
\end{aligned}
\tag{83}
$$

As in the KN case above, for the timelike case here we only investigate the stable ones; that is when (83) satisfies conditions (12) and (78). These conditions yield four types of solutions, the first two of which are

$$
\begin{aligned}
E_{a,b} &= \sqrt{\dfrac{e^{-2k/r_{SO}}\left[-2a^4 M\mathcal{C}e^{3k/r_{SO}}\left(k-r_{SO}\right) - A + r_{SO}^4\left(B \pm 2\sqrt{N}\right)\right]}{D}}, \\
\Phi_{a,b} &= -\frac{e^{-k/r_{SO}}E_{a,b}}{aHM(k-r_{SO})} \\
&\quad \times \left[a^4 M^2 e^{2k/r_{SO}}(k-r_{SO})\left[k\left(c+r_{SO}^2\right)+r_{SO}\left(\mathcal{C}-r_{SO}^2\right)\right] + F + r_{SO}^6\sqrt{\frac{G}{r_{SO}^8}}\right],
\end{aligned}
\tag{84}
$$

where

$$A \equiv a^2 e^{2k/r_{SO}} \left\{ M^2 \left[r_{SO}^2 \left(k^2 + 5\mathcal{C} \right) + k^2 \mathcal{C} - 2k\mathcal{C}r_{SO} + 4kr_{SO}^3 - 5r_{SO}^4 \right] \right.$$

$$\left. Mr_{SO}^3 e^{k/r_{SO}} [3r_{SO}(r_{SO} - k) - 4\mathcal{C}] + \mathcal{C}r_{SO}^4 e^{2k/r_{SO}} \right\}, \tag{85}$$

$$B \equiv e^{k/r_{SO}} \left(r_{SO}e^{k/r_{SO}} - 2M \right)^2 \left[r_{SO} \left(r_{SO}e^{k/r_{SO}} - 3M \right) + kM \right], \tag{86}$$

$$N \equiv \frac{1}{r_{SO}^8} \left\{ a^2 M^2 e^{3k/r_{SO}} (k - r_{SO})^2 \left[\left(a^2 + r_{SO}^2 \right) e^{k/r_{SO}} - 2Mr_{SO} \right]^2 \right\}$$

$$\times \left\{ \mathcal{C}e^{k/r_{SO}} \left(a^2 \mathcal{C} - r_{SO}^4 \right) + Mr_{SO}^2 \left[-k \left(\mathcal{C} + r_{SO}^2 \right) + 3\mathcal{C}r_{SO} + r_{SO}^3 \right] \right\}, \tag{87}$$

$$D \equiv r_{SO}^4 \left\{ 4a^2 M e^{k/r_{SO}} (k - r_{SO}) + \left[r_{SO} \left(r_{SO}e^{k/r_{SO}} - 3M \right) + kM \right]^2 \right\}, \tag{88}$$

$$F \equiv a^2 M^2 r_{SO}^2 e^{k/r_{SO}} (k - r_{SO}) \left\{ e^{k/r_{SO}} \left[k \left(\mathcal{C} + r_{SO}^2 \right) - r_{SO} \left(\mathcal{C} + 3r_{SO}^2 \right) \right] + 4Mr_{SO}^2 \right\}, \tag{89}$$

$$G \equiv a^2 M^2 e^{3k/r_{SO}} (k - r_{SO})^2 \left[\left(a^2 + r_{SO}^2 \right) e^{k/r_{SO}} - 2Mr_{SO} \right]^2$$

$$\times \left\{ \mathcal{C}e^{k/r_{SO}} \left(a^2 \mathcal{C} - r_{SO}^4 \right) + Mr_{SO}^2 \left[-k \left(\mathcal{C} + r_{SO}^2 \right) + 3\mathcal{C}r_{SO} + r_{SO}^3 \right] \right\}, \tag{90}$$

$$H \equiv a^2 e^{k/r_{SO}} \left[r_{SO} \left(\mathcal{C}r_{SO}e^{k/r_{SO}} - M\mathcal{C} + Mr_{SO}^2 \right) - kM \left(\mathcal{C} + r_{SO}^2 \right) \right] - r_{SO}^4 \left(r_{SO}e^{k/r_{SO}} - 2M \right)^2. \tag{91}$$

The third and fourth solutions are related through

$$(E_{c,d}, \Phi_{c,d}) = -(E_{a,b}, \Phi_{a,b}). \tag{92}$$

1. **Analytical Solutions**

From $V(u^2) = 0$ the roots $w_{1,2} \equiv u^2$ can be found as

$$w_{1,2} = \frac{a^2 \left(1 - E^2 \right) + \mathcal{C} + \Phi^2 \mp \sqrt{\left[a^2 \left(1 - E^2 \right) + \mathcal{C} + \Phi^2 \right]^2 - 4a^2 \mathcal{C} \left(1 - E^2 \right)}}{2a^2 \left(1 - E^2 \right)}. \tag{93}$$

Orbit	Mk	a/M	r_{SO}/M	C/M^2	E	Φ/M	u_0	$\Delta\phi$
(a)	0	0.3	6	8	0.937	1.733	0.852	6.535
(b)	0.1	0.3	6	8	0.936	1.576	0.873	6.535
(c)	0.5	0.3	6	8	0.93	0.857	0.956	6.537

TABLE XII: Parameters of the STO around a non-extremal regular rotating black hole.

As before, for bound orbits we have $E^2 < 1$ and $0 \leq w \leq w_1 \leq 1 < w_2$. The analytical solutions for $\{\theta(\lambda), \phi(\lambda), t(\lambda)\}$ are

$$\theta(\lambda) = \arccos\left[\sqrt{w_1}\,\mathrm{sn}(a\sqrt{(1-E^2)\,w_2}\lambda, \kappa)\right], \tag{94}$$

$$\phi(\lambda) = \frac{\Phi}{a\sqrt{(1-E^2)\,w_2}}\Pi(\Psi, w_1, \kappa) + \frac{a}{\Delta}\left(2MrEe^{-k/r} - a\Phi\right)\lambda, \tag{95}$$

$$t(\lambda) = -\frac{aE}{\sqrt{(1-E^2)w_2}}\left[(1-w_2)F(\Psi, \kappa) + w_2 E(\Psi, \kappa)\right]$$
$$+ \frac{1}{\Delta}\left[E(r^2+a^2)^2 - 2Mra\Phi e^{-k/r}\right]\lambda, \tag{96}$$

where

$$\Psi \equiv \mathrm{am}(a\sqrt{(1-E^2)\,w_2}\lambda, \kappa), \tag{97}$$
$$\kappa \equiv \sqrt{\frac{w_1}{w_2}}.$$

The period of $\theta(\lambda)$ is

$$\Delta\lambda = \frac{4}{a\sqrt{(1-E^2)\,w_2}}K(\kappa). \tag{98}$$

The change in ϕ and t for one period are

$$\Delta\phi = \frac{4}{a\sqrt{(1-E^2)\,w_2}}\left[\frac{\Phi}{a}\Pi(w_1, \kappa) + \frac{2MrEe^{-k/r} - a\Phi}{\Delta}K(\kappa)\right], \tag{99}$$

$$\Delta t = -\frac{4}{a\sqrt{(1-E^2)\,w_2}}\Bigg\{-a\left[(1-w_2)K(\kappa) + w_2 E(\kappa)\right]$$
$$+ \left[\frac{E(r^2+a^2)^2 - 2Mra\Phi e^{-k/r}}{a\Delta}\right]K(\kappa)\Bigg\}. \tag{100}$$

2. Selected orbits

From the derived solutions (94)-(96), we can visualize certain timelike orbits. We present
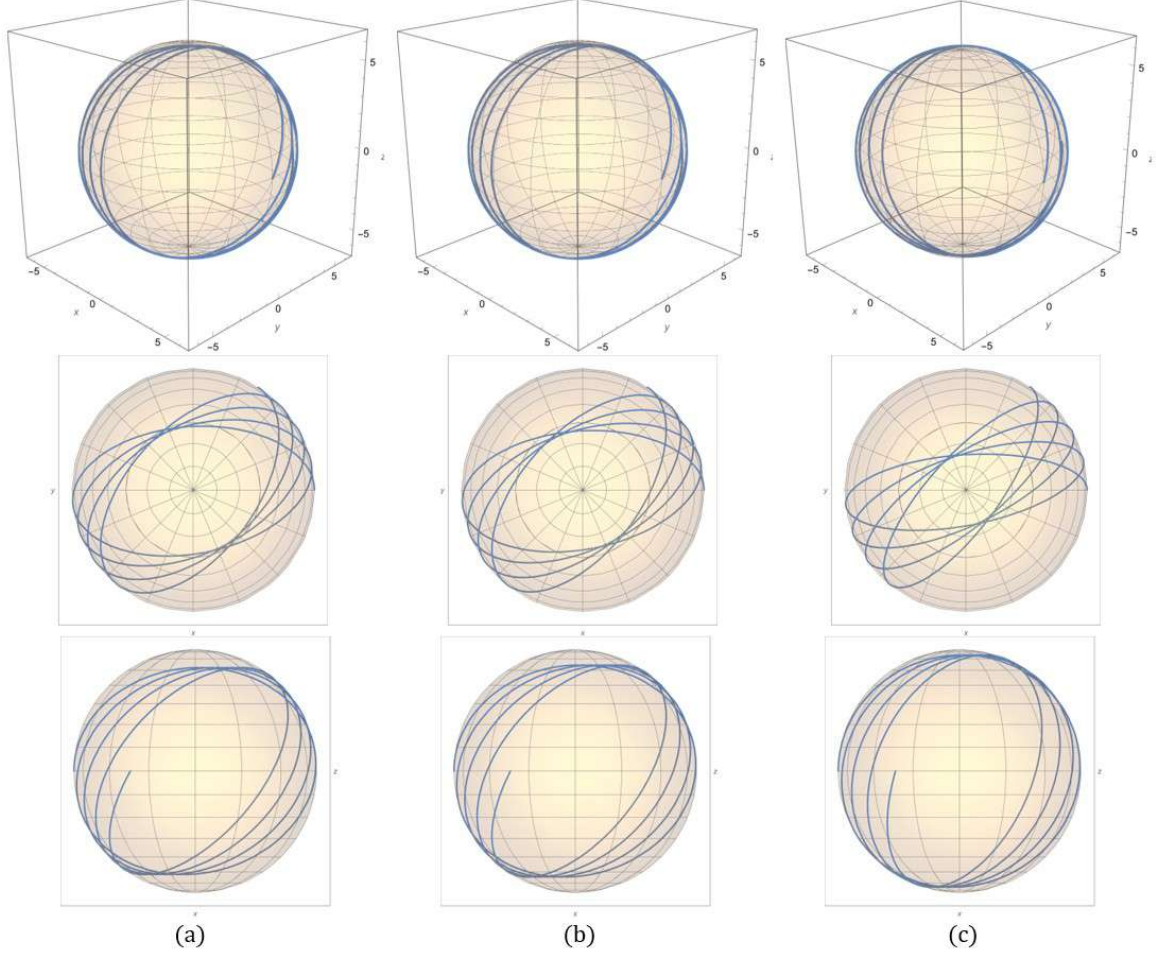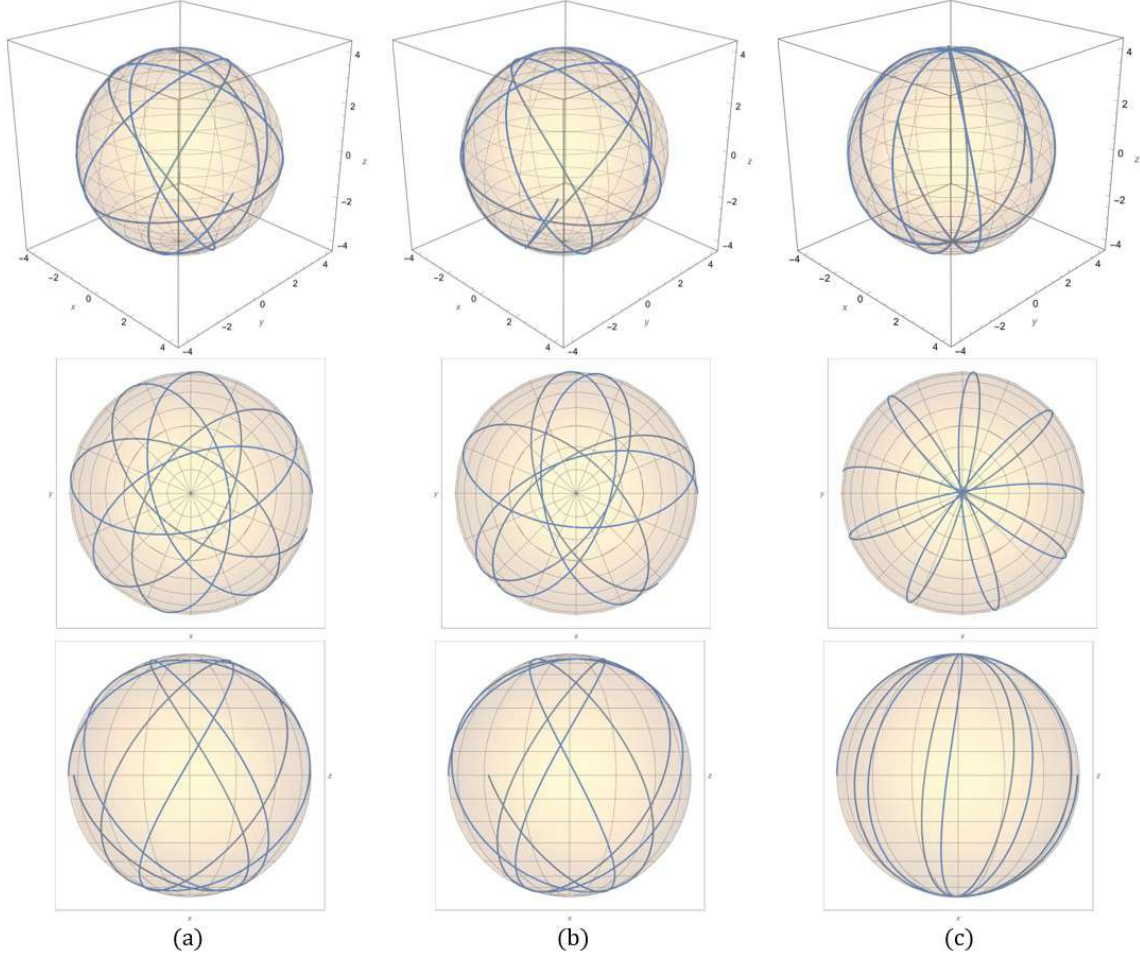
FIG. 17: Spherical timelike orbits around non-extremal regular black hole case in the $(x - y - z)$ as well as the projective $x - y$ and $x - z$ planes. The direction of the black hole's rotation is from west to east. (a) $\Phi/M = 1.733$ and $Mk = 0$, (b) $\Phi/M = 1.576$ and $Mk = 0.1$, (c) $\Phi/M = 0.857$ and $Mk = 0.5$.

the STOs for non-extremal cases in Fig. 17, accompanied by parameters detailed in Table XII. Analogous to the Kerr-Newman (KN) and regular SPO scenarios, there is an inclination for larger values of k to draw the orbit trajectory nearer to the pole, resulting in a notably expanded latitudinal oscillation amplitude. Distinctive plots for STOs encircling extremal black holes are showcased in Fig. 18, with corresponding parameters outlined in Table XIII. Here, we observe a distinctive orbit morphology: with increasing k, the trajectories depicted in the projective $x - y$ plane exhibit diminishing "leaf" shapes and augmented latitudinal oscillation amplitudes. Lastly, we delineate the orbits surrounding naked or no-horizon scenarios in Fig. 19, accompanied by parameters expounded in Table XIV.

Orbit	Mk	a/M	r_{SO}/M	C/M^2	E	Φ/M	u_0	$\Delta\phi$
(a)	0	1	4	8	0.918	0.918	0.95	7.78
(b)	0.1	0.8998	4	8	0.918	0.819	0.96	7.645
(c)	0.5	0.472	4	8	0.918	0.043	0.999	7.023

TABLE XIII: Parameters of the STO around the extremal regular rotating black hole.

(a) (b) (c)

FIG. 18: Spherical timelike orbits around extremal regular black hole in the $(x - y - z)$ as well as the projective $x - y$ and $x - z$ planes. The direction of the black hole's rotation is from west to east. (a) $\Phi/M = 0.918$ and $k = 0$, (b) $\Phi/M = 0.819$ and $k = 0.1$, (c) $\Phi/M = 0.043$ and $k = 0.5$.

3. Innermost Stable Spherical Orbits

Using a similar method with Kerr-Newman black holes, we can get the ISSO as a function of Carter's constant. The ISSO for the Ghosh BH presents some interesting features: the

Orbit	Mk	a/M	r/M	C/M^2	E	Φ/M	u_0	$\Delta\phi$
(a)	0.1	1	8	8	0.943	1.596	0.869	6.79
(b)	0.5	1	8	8	0.941	1.211	0.918	6.798

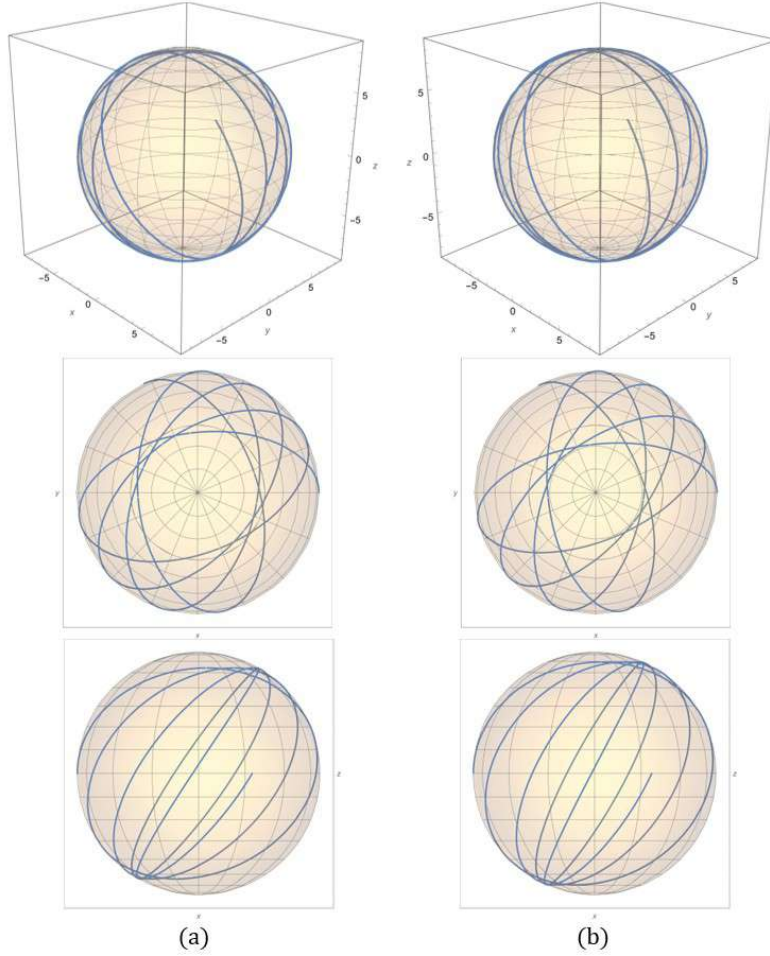TABLE XIV: Parameters of the STO around naked regularity.

(a)   (b)

FIG. 19: Spherical timelike orbits around no-horizon spacetime in the $(x - y - z)$ as well as the projective $x - y$ and $x - z$ planes. The direction of the black hole's rotation is from west to east. (a) $\Phi/M = 1.596$ and $k = 0.1$, (b) $\Phi/M = 1.211$ and $k = 0.5$.

branches are discontinuous. Some of them stop at some finite values, as we shall see below. The form of the regular metric is such that there exist some ranges of C/M^2 which have complex r_{ISSO}.

For a non-extremal case the result is shown in Fig. 20 with $a = 0.7M$ and $k = 0.1M$. Both branches are observable (outside the horizons). The lower branch starts at $r_{ISSO}/M \sim 2.92$

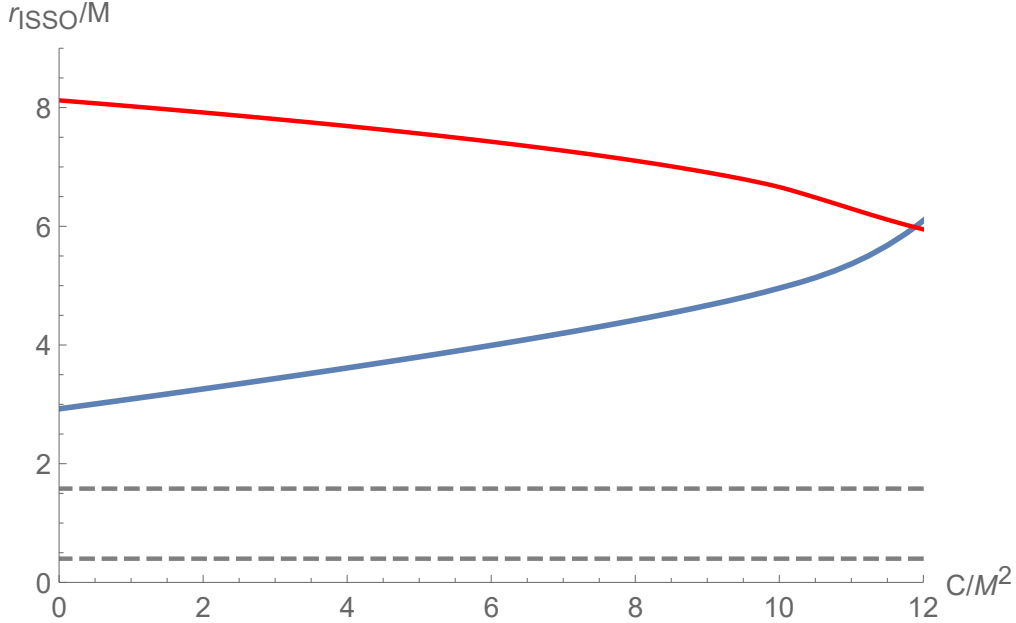FIG. 20: r_{ISSO} as a function of Carter's constant for a non-extremal regular black hole when $a = 0.7M$ and $k = 0.1M$. The red and blue lines are the r_{isso} from the $\pm$ sign in eq. 84, and black dashed lines are the event horizons.

while the upper one starts $r_{ISSO}/M \sim 8.12$. Unlike the KN case, here the two branches do not merge and stop at C_{crit}, but they somehow cross as can be seen from the figure. The crossing value is around $r_{ISSO}/M \sim 6.09$ at $C/M^2 \sim 12$. A more interesting case happens for the extremal BH. In Fig. 21 it can be seen that the lower branch starts at the extremal horizon for $C/M^2 = 0$, then goes up as usual. However, instead of merging or crossing with the upper branch, the two branches do not merge at a single C value. The upper branch stops being real at around $r_{ISSO}/M \sim 6.55$. It only exists between $0 \le C/M^2 \lesssim 11$. Finally, the no-horizon case is the most interesting of all. As can be seen from Fig. 22, the lower branch ceases to exist up until $C/M^2 \sim 4.4$, at $r_{ISSO} \sim 2.23$. On the other hand, the upper branch starts with $r_{ISSO}/M \sim 8.8$ and it stops being real around $r_{ISSO} \lesssim 5.98$ at $C/M^2 \sim 11$. A typical ISSO trajectory is shown in Fig. 23. This is an example of ISSO in a no-horizon case, with $a/M = 0.95$, $k/M = 0.1$, and $C/M^2 = 10$. The corresponding ISSO radius is $r_{ISSO}/M \sim 7.08$.
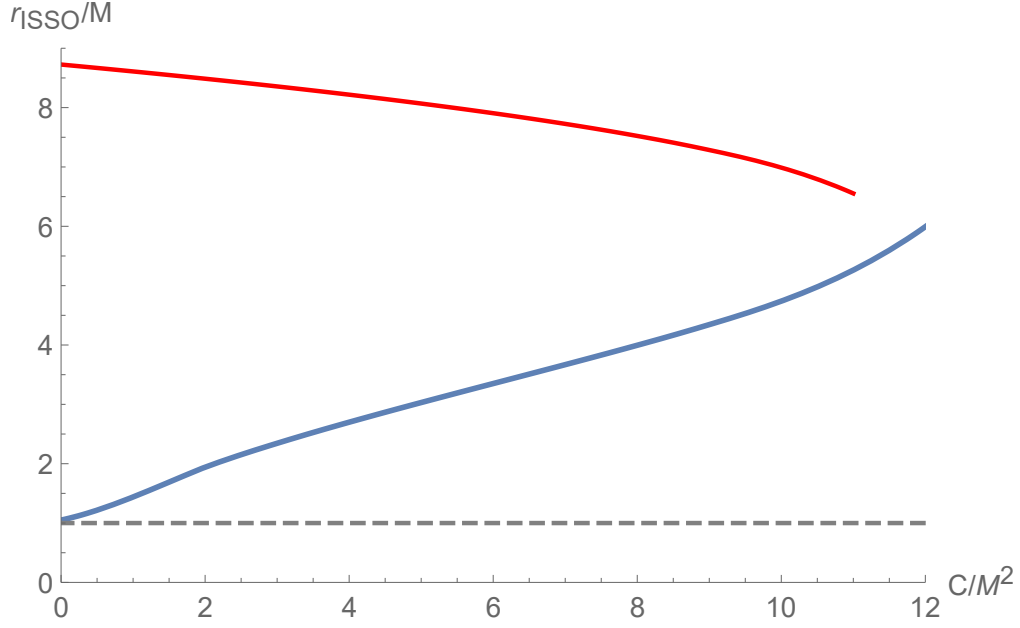
FIG. 21: r_{ISSO} as a function of Carter's constant for an extremal regular black hole when $a = 0.8998M$ and $k = 0.1M$. The red and blue lines are the r_{isso} from $\pm$ sign in eq. 84, and the black dashed line is the event horizon.
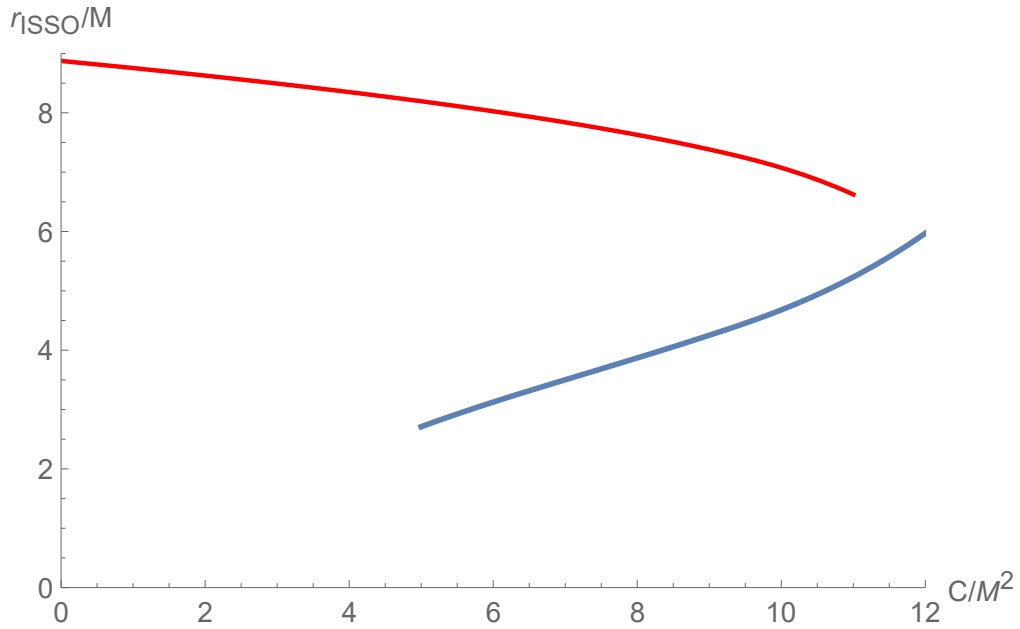

FIG. 22: r_{ISSO} as a function of Carter's constant for a naked regular black hole when $a = 0.95M$ and $k = 0.1M$. The red and blue lines are the r_{isso} from the $\pm$ sign in eq. 84.
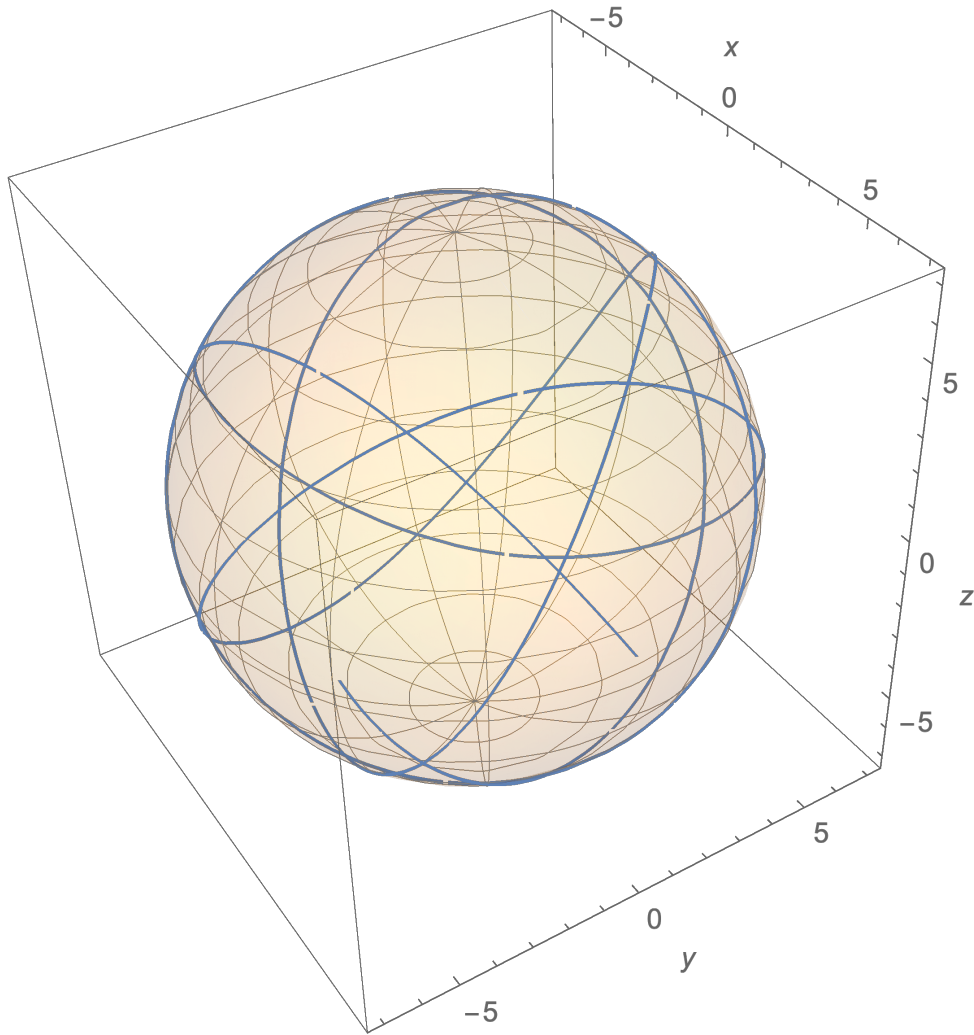
FIG. 23: The ISSO trajectory around the no-horizon case of Ghosh BH (based on the data in Fig. 22). Here $C/M^2 = 10$, $a/M = 0.95$, and $k/M = 0.1$. The corresponding ISSO radius is $r_{ISSO} \sim 7.075M$.

IV. CONCLUSION

In this study we expand upon Teo's seminal analysis of spherical orbits [33, 34], delving into the charged rotating black holes. Specifically, our focus lies on two distinct models: the Kerr-Newman and the Ghosh black holes, the latter representing a novel regular rotating black hole obtained by conducting the Newman-Janis transformation of a spherically-symmetric regular metric. Notably, the metric described by Eq. (56) reduces to Kerr at $k \to 0$ and to the Kerr-Newman at $r >> k$. Leveraging exact analytical solutions in terms of Mino parameters, we explore the presence of both spherical photon orbits (SPOs) and

spherical timelike orbits (STOs) in these models. Noteworthy is our assumption that the direction of rotation for the black hole is from west to east, with all orbits originating from the equatorial plane and progressing northward.

In the case of Kerr-Newman black holes we found that, similar to the Kerr case, all observable SPOs prove to be unstable under radial perturbation. This instability is evident from the effective potential $V_{eff} \equiv -R(r)$, where all SPOs satisfy Eq. (15). With the introduction of charge, the $C - r$ and $\Phi - r$ plots undergo a shift to the right, while the maximum value of the former decreases compared to Kerr. This shift indicates a higher concentration of photon trajectories around the equatorial plane. This concentration is further confirmed by the directional velocity θ and angular momentum Φ which decrease and increase, respectively, as the charge Q increases. Additionally, it requires more latitudinal oscillations to form a closed trajectory. Notably, the charge Q can reorient the photon's motion about the z-axis of the black hole. For $\Phi = -M$, the initially retrograde orbit transitions to prograde motion. This transition occurs at $Q/M = 0.6$ for both non-extremal and extremal black holes. Furthermore, we observe a photon boomerang trajectory, $\Delta\phi = \pi$, in the extremal case. This happens in the extremal case, occurring at low charge values $Q = 0.02528M$, and $\Phi = 0$. Here we do not attempt to investigate the stable SPOs, which are available only for Kerr naked singularity. Note that there has been extensive discussions on the SPOs around the Kerr naked singularities (KNSs) [75–77]. The existence of Kerr superspinars might be a signature for the string theory [78].

Exploring geodesics around Ghosh black holes raises the intriguing question of whether stable SPOs exist outside the horizon. This is a nonsingular rotating black hole, parametrized by an additional parameter k. However, our investigation yielded disappointing results, as all SPOs around regular black holes prove to be unstable. Additionally, we observed that the condition $Mk >> 1$ is incompatible with both non-zero a/M and observability criteria $r_{SO} > r_h$. In the non-extremal case, this circumstance renders photon orbits predominantly equatorial. However, in the extremal case, where $Mk \lesssim 0.5$, a complete SPO exists. Note that in this BH the extremality can be achieved by either a/M or Mk. We identified an approximate photon boomerang in this extremal case, with $k = 0.05$ and $\Phi = -0.07$. Since regular black holes lack naked singularities, the absence of a horizon in the metric poses no physical paradox. This so-called "*no-horizon*" condition may conceptually align with that of a horizonless ultracompact star. Digging further into our investigation

around no-horizon condition, we discovered that photons can orbit spherically under stable conditions, albeit only when $\Phi \leq 0$. This finding highlights the presence of the Lens-Thirring effect.

For stable spherical timelike orbits (STOs), both KN and Ghosh BHs allow orbits to exist outside their horizons. In the KN scenario, bound orbits occur when $E^2 < 1$, while $E^2 = 1$ signifies a marginally bound orbit. Unlike null orbits, timelike orbits do not exhibit retrograde-prograde switching. In the Ghosh case, higher values of k drive trajectories closer to the pole, resulting in larger latitudinal oscillation amplitudes. Notably, the concept of innermost stable spherical orbits (ISSOs) in spherical trajectory parallels the innermost stable circular orbits (ISCOs) in equitorial motion. The ISSO radius in KN can be determined by solving Eqs. (53)-(54). These solutions, depicted in Fig. 8, manifest as two branches of $r_{ISSO}(C)$. A typical ISSO trajectory in the KN BH, illustrated in Fig. 9, appears densely concentrated around the equator initially, gradually filling the entire solid angle as it completes one latitudinal oscillation. In contrast, ISSO behavior in the Ghosh BH presents intriguing nuances. Unlike the KN case, the nonsingular nature of the Ghosh metric causes ISSO branches to terminate at finite values, as depicted in Figs. 20-22. A representative ISSO trajectory is shown in Fig. 23. As a closing statement in this paragraph we should briefly comment on this ISSO issue. It is evident that in both types of black holes under examination, the radial potential $R(r)$ is at least quartic in r. This leads to two roots for each solution of $R'' = 0$, hence the presence of two branches. The lower branch in each r_{ISSO} vs C plot should be the one that represents the "true" ISSO, as the name by itself stands.

Finally, we should also comment on the phenomenological aspects of our results. Our theoretical findings hold significant potential for astrophysical applications. Firstly, the prevalence of unstable spherical photon orbits (SPOs) in our study is advantageous for detection purposes. This diversity of unstable SPOs around various rotating black hole models contributes to a more comprehensive understanding and visualization of black holes. In particular, the calculation of the photon ring's two-point correlation function, reliant on unstable SPOs as demonstrated for the Kerr black hole in [79], holds promise for future validation through experiments like the upcoming Event Horizon Telescope (EHT) project [40]. Secondly, our study sheds light on the crucial information regarding stable spherical timelike orbits (STOs). Being the asymptotic trajectories of homoclinic orbits [80, 81], STOs carry fundamental significance, for example in the context of the gravitational waves analysis from

extreme mass-ratio inspirals (EMRIs)[34, 82–84]. Additionally, our results pave the way for further investigations, such as exploring the gravitational redshift/blueshift emission from STOs around Ghosh black holes, a research avenue previously explored for Kerr and Kerr-de Sitter black holes in [85]. The other aspect is to explore the black hole merger estimate as presented in [86]. It is also interesting to investigate how our results fit into observational constraints by considering the black hole shadow [87, 88]. We leave this for our further investigations.

Statement of the Conflict of Interest

All authors hereby declare that we do not have any conflict of interest.

Data Availability Statement

Data sharing is not applicable to this article as no data sets were generated or analyzed during the current study.

---

[1] K. Akiyama *et al.* [Event Horizon Telescope], "First M87 Event Horizon Telescope Results. I. The Shadow of the Supermassive Black Hole," Astrophys. J. Lett. **875** (2019), L1 [arXiv:1906.11238 [astro-ph.GA]]; K. Akiyama *et al.* [Event Horizon Telescope], "First M87 Event Horizon Telescope Results. VI. The Shadow and Mass of the Central Black Hole," Astrophys. J. Lett. **875** (2019) no.1, L6 [arXiv:1906.11243 [astro-ph.GA]].

[2] K. Akiyama *et al.* [Event Horizon Telescope], "First Sagittarius A* Event Horizon Telescope Results. I. The Shadow of the Supermassive Black Hole in the Center of the Milky Way," Astrophys. J. Lett. **930** (2022) no.2, L12 [arXiv:2311.08680 [astro-ph.HE]]; K. Akiyama *et al.* [Event Horizon Telescope], "First Sagittarius A* Event Horizon Telescope Results. V. Testing Astrophysical Models of the Galactic Center Black Hole," Astrophys. J. Lett. **930** (2022) no.2, L16 [arXiv:2311.09478 [astro-ph.HE]]; K. Akiyama *et al.* [Event Horizon Telescope], "First Sagittarius A* Event Horizon Telescope Results. VI. Testing the Black Hole Metric," Astrophys. J. Lett. **930** (2022) no.2, L17 [arXiv:2311.09484 [astro-ph.HE]].

[3] S. M. Carroll, "Spacetime and Geometry: An Introduction to General Relativity," Cambridge University Press, Cambridge (2019)

[4] F. S. Khoo and Y. C. Ong, "Lux in obscuro: Photon Orbits of Extremal Black Holes Revisited," Class. Quant. Grav. **33** (2016) no.23, 235002 [erratum: Class. Quant. Grav. **34** (2017) no.21, 219501] arXiv:1605.05774 [gr-qc].

[5] P. Pradhan and P. Majumdar, "Circular Orbits in Extremal Reissner Nordstrom Spacetimes," Phys. Lett. A **375** (2011), 474-479 [arXiv:1001.0359 [gr-qc]].

[6] Bardeen, J. M. 1973, in Les Houches Summer School of Theoretical Physics: Black Holes

[7] J. P. Luminet, "Image of a spherical black hole with thin accretion disk," Astron. Astrophys. **75** (1979), 228-235

[8] H. Falcke, F. Melia and E. Agol, "Viewing the shadow of the black hole at the galactic center," Astrophys. J. Lett. **528** (2000), L13 [arXiv:astro-ph/9912263 [astro-ph]].

[9] T. Johannsen and D. Psaltis, "Testing the No-Hair Theorem with Observations in the Electromagnetic Spectrum: II. Black-Hole Images," Astrophys. J. **718** (2010), 446-454 [arXiv:1005.1931 [astro-ph.HE]].

[10] R. Kumar and S. G. Ghosh, "Black Hole Parameter Estimation from Its Shadow," Astrophys. J. **892** (2020), 78 [arXiv:1811.01260 [gr-qc]].

[11] M. Afrin and S. G. Ghosh, "Testing Horndeski Gravity from EHT Observational Results for Rotating Black Holes," Astrophys. J. **932** (2022) no.1, 51 [arXiv:2110.05258 [gr-qc]].

[12] R. P. Kerr, "Gravitational field of a spinning mass as an example of algebraically special metrics," Phys. Rev. Lett. **11** (1963), 237-238

[13] E. T. Newman, R. Couch, K. Chinnapared, A. Exton, A. Prakash and R. Torrence, "Metric of a Rotating, Charged Mass," J. Math. Phys. **6** (1965), 918-919

[14] S. G. Ghosh and M. Afrin, "An Upper Limit on the Charge of the Black Hole Sgr A* from EHT Observations," Astrophys. J. **944** (2023) no.2, 174 [arXiv:2206.02488 [gr-qc]].

[15] S. Vagnozzi, R. Roy, Y. D. Tsai, L. Visinelli, M. Afrin, A. Allahyari, P. Bambhaniya, D. Dey, S. G. Ghosh and P. S. Joshi, *et al.* "Horizon-scale tests of gravity theories and fundamental physics from the Event Horizon Telescope image of Sagittarius A," Class. Quant. Grav. **40** (2023) no.16, 165007 [arXiv:2205.07787 [gr-qc]].

[16] M. Khodadi and G. Lambiase, "Probing Lorentz symmetry violation using the first image of Sagittarius A*: Constraints on standard-model extension coefficients," Phys. Rev. D **106** (2022) no.10, 104050 [arXiv:2206.08601 [gr-qc]].

[17] R. Kumar Walia, S. G. Ghosh and S. D. Maharaj, "Testing Rotating Regular Metrics with EHT Results of Sgr A*," Astrophys. J. **939** (2022) no.2, 77 [arXiv:2207.00078 [gr-qc]].

[18] R. Kumar Walia, "Observational predictions of LQG motivated polymerized black holes and constraints from Sgr A* and M87*," JCAP **03** (2023), 029 [arXiv:2207.02106 [gr-qc]].

[19] A. Uniyal, R. C. Pantig and A. Övgün, "Probing a non-linear electrodynamics black hole with thin accretion disk, shadow, and deflection angle with M87* and Sgr A* from EHT," Phys. Dark Univ. **40** (2023), 101178 [arXiv:2205.11072 [gr-qc]].

[20] B. Carter, "Global structure of the Kerr family of gravitational fields," Phys. Rev. **174** (1968), 1559-1571

[21] D. C. Wilkins, "Bound Geodesics in the Kerr Metric," Phys. Rev. D **5** (1972), 814-822

[22] M. Johnston and R. Ruffini, "Generalized Wilkins effect and selected orbits in a Kerr-Newman geometry," Phys. Rev. D **10** (1974), 2324-2329

[23] Z. Stuchlik, (1981). "The radial motion of photons in Kerr metric," Bull. Astron. Inst. Czechosl. **32** (1981), 40–52.

[24] M. Calvani, F. De Felice and L. Nobili, "PHOTON TRAJECTORIES IN THE KERR-NEWMAN METRIC," J. Phys. A **13** (1980), 3213-3219

[25] H. Goldstein, "Numerical calculation of bound geodesics in the Kerr metric," Z. Phys. **271**, 275–279 (1974).

[26] Y. Mino, "Perturbative approach to an orbital evolution around a supermassive black hole," Phys. Rev. D **67** (2003), 084027 [arXiv:gr-qc/0302075 [gr-qc]].

[27] R. Fujita and W. Hikida, "Analytical solutions of bound timelike geodesic orbits in Kerr spacetime," Class. Quant. Grav. **26** (2009), 135002 [arXiv:0906.1420 [gr-qc]].

[28] E. Battista and G. Esposito, "Geodesic motion in Euclidean Schwarzschild geometry," Eur. Phys. J. C **82** (2022) no.12, 1088 [arXiv:2202.03763 [gr-qc]].

[29] E. Hackmann, C. Lammerzahl, V. Kagramanova and J. Kunz, "Analytical solution of the geodesic equation in Kerr-(anti) de Sitter space-times," Phys. Rev. D **81** (2010), 044020 [arXiv:1009.6117 [gr-qc]].

[30] E. Hackmann and H. Xu, "Charged particle motion in Kerr-Newmann space-times," Phys. Rev. D **87** (2013) no.12, 124030 [arXiv:1304.2142 [gr-qc]].

[31] C. Lämmerzahl and E. Hackmann, "Analytical Solutions for Geodesic Equation in Black Hole Spacetimes," Springer Proc. Phys. **170** (2016), 43-51 [arXiv:1506.01572 [gr-qc]].

[32] C. Y. Wang, D. S. Lee and C. Y. Lin, "Null and timelike geodesics in the Kerr-Newman black hole exterior," Phys. Rev. D **106** (2022) no.8, 084048 [arXiv:2208.11906 [gr-qc]].

[33] E. Teo, "Spherical photon orbits around a Kerr black hole," Gen. Rel. Grav. **35** (2003) 1909.

[34] E. Teo, "Spherical orbits around a Kerr black hole," Gen. Rel. Grav. **53** (2021) no.1, 10 [arXiv:2007.04022 [gr-qc]].

[35] R. Grossman, J. Levin and G. Perez-Giz, "The harmonic structure of generic Kerr orbits," Phys. Rev. D **85** (2012), 023012 [arXiv:1105.5811 [gr-qc]].

[36] A. Tavlayan and B. Tekin, "Exact Formulas for Spherical Photon Orbits Around Kerr Black Holes," Phys. Rev. D **102** (2020) no.10, 104036 [arXiv:2009.07012 [gr-qc]].

[37] A. Tavlayan and B. Tekin, "Radii of spherical timelike orbits around Kerr black holes," Phys. Rev. D **104** (2021) no.12, 124059 [arXiv:2110.13070 [gr-qc]].

[38] S. Hod, "Marginally bound (critical) geodesics of rapidly rotating black holes," Phys. Rev. D **88** (2013) no.8, 087502 [arXiv:1707.05680 [gr-qc]].

[39] D. N. Page, "Photon boomerang in a nearly extreme Kerr metric," Class. Quant. Grav. **39** (2022) no.13, 135015 [arXiv:2106.13262 [gr-qc]].

[40] A. Anjum, M. Afrin and S. G. Ghosh, "Investigating effects of dark matter on photon orbits and black hole shadows," Phys. Dark Univ. **40** (2023), 101195

[41] A. Das, A. Saha and S. Gangopadhyay, "Investigation of circular geodesics in a rotating charged black hole in the presence of perfect fluid dark matter," Class. Quant. Grav. **38** (2021) no.6, 065015 [arXiv:2009.03644 [gr-qc]].

[42] F. Atamurotov, A. Abdujabbarov and W. B. Han, "Effect of plasma on gravitational lensing by a Schwarzschild black hole immersed in perfect fluid dark matter," Phys. Rev. D **104**

(2021) no.8, 084015

[43] F. Atamurotov, U. Papnoi and K. Jusufi, "Shadow and deflection angle of charged rotating black hole surrounded by perfect fluid dark matter," Class. Quant. Grav. **39** (2022) no.2, 025014 [arXiv:2104.14898 [gr-qc]].

[44] X. Hou, Z. Xu and J. Wang, "Rotating Black Hole Shadow in Perfect Fluid Dark Matter," JCAP **12** (2018), 040 [arXiv:1810.06381 [gr-qc]].

[45] S. Haroon, M. Jamil, K. Jusufi, K. Lin and R. B. Mann, "Shadow and Deflection Angle of Rotating Black Holes in Perfect Fluid Dark Matter with a Cosmological Constant," Phys. Rev. D **99** (2019) no.4, 044015 [arXiv:1810.04103 [gr-qc]].

[46] A. Das, A. Saha and S. Gangopadhyay, "Study of circular geodesics and shadow of rotating charged black hole surrounded by perfect fluid dark matter immersed in plasma," Class. Quant. Grav. **39** (2022) no.7, 075005 [arXiv:2110.11704 [gr-qc]].

[47] B. Narzilloev, J. Rayimbaev, S. Shaymatov, A. Abdujabbarov, B. Ahmedov and C. Bambi, "Dynamics of test particles around a Bardeen black hole surrounded by perfect fluid dark matter," Phys. Rev. D **102** (2020) no.10, 104062 [arXiv:2011.06148 [gr-qc]].

[48] A. D. Sakharov, "Nachal'naia stadija rasshirenija Vselennoj i vozniknovenije neodnorodnosti raspredelenija veshchestva (Initial stage of an expanding universe and appearence of a nonuniform distribution of matter)," Sov. Phys. JETP **22** (1966), 241.

[49] J. Bardeen, "Non-Singular General-Relativistic Gravitational Collapse," Proc. Int. Conf. GR5, Tbilisi **174** (1968).

[50] E. Ayon-Beato and A. Garcia, "Regular black hole in general relativity coupled to nonlinear electrodynamics," Phys. Rev. Lett. **80** (1998), 5056-5059 [arXiv:gr-qc/9911046 [gr-qc]].

[51] E. Ayon-Beato and A. Garcia, "The Bardeen model as a nonlinear magnetic monopole," Phys. Lett. B **493** (2000), 149-152 [arXiv:gr-qc/0009077 [gr-qc]].

[52] S. Ansoldi, "Spherical black holes with regular center: A Review of existing models including a recent realization with Gaussian sources," [arXiv:0802.0330 [gr-qc]].

[53] C. Bambi and L. Modesto, "Rotating regular black holes," Phys. Lett. B **721** (2013), 329-334 [arXiv:1302.6075 [gr-qc]].

[54] B. Toshmatov, B. Ahmedov, A. Abdujabbarov and Z. Stuchlik, "Rotating Regular Black Hole Solution," Phys. Rev. D **89** (2014) no.10, 104017 [arXiv:1404.6443 [gr-qc]].

[55] S. G. Ghosh, "A nonsingular rotating black hole," Eur. Phys. J. C **75** (2015) no.11, 532

[arXiv:1408.5668 [gr-qc]].

[56] M. Amir and S. G. Ghosh, "Shapes of rotating nonsingular black hole shadows," Phys. Rev. D **94** (2016) no.2, 024054 [arXiv:1603.06382 [gr-qc]].

[57] R. Kumar, A. Kumar and S. G. Ghosh, "Testing Rotating Regular Metrics as Candidates for Astrophysical Black Holes," Astrophys. J. **896** (2020) no.1, 89 [arXiv:2006.09869 [gr-qc]].

[58] A. Kumar, S. G. Ghosh and S. D. Maharaj, "Nonsingular black hole chemistry," Phys. Dark Univ. **30** (2020), 100634 [arXiv:2106.15925 [gr-qc]].

[59] R. Kumar and S. G. Ghosh, "Photon ring structure of rotating regular black holes and no-horizon spacetimes," Class. Quant. Grav. **38** (2021) no.8, 8 [arXiv:2004.07501 [gr-qc]].

[60] I. S. Gradshteyn and I. M. Ryzhik; A. Jeffrey, ed., "Table of Integrals, Series, and Products, 5th ed.," Academic Press, London (1994).

[61] M. Abramowitz and I. A. Stegun, eds., "Handbook of Mathematical Functions," Dover, New York (1972).

[62] P. F. Byrd and M. D. Friedman, "Handbook of Elliptic Integrals for Engineers and Scientists, 2nd ed.," Springer, Berlin (1971).

[63] J. M. Bardeen, W. H. Press and S. A. Teukolsky, "Rotating black holes: Locally nonrotating frames, energy extraction, and scalar synchrotron radiation," Astrophys. J. **178** (1972), 347

[64] A. Druart, "The Motion of Test Bodies around Kerr Black Holes," [arXiv:2307.02589 [gr-qc]].

[65] L. Balart and E. C. Vagenas, "Regular black holes with a nonlinear electrodynamics source," Phys. Rev. D **90** (2014) no.12, 124045 [arXiv:1408.0306 [gr-qc]].

[66] H. Culetu, "On a regular charged black hole with a nonlinear electric source," Int. J. Theor. Phys. **54** (2015) no.8, 2855-2863 [arXiv:1408.3334 [gr-qc]].

[67] E. T. Newman and A. I. Janis, "Note on the Kerr spinning particle metric," J. Math. Phys. **6** (1965), 915-917

[68] H. S. Ramadhan, M. F. Ishlah, F. P. Pratama and I. Alfredo, "Strong lensing and shadow of Ayon-Beato–Garcia (ABG) nonsingular black hole," Eur. Phys. J. C **83** (2023) no.6, 465 [arXiv:2303.10921 [gr-qc]].

[69] R. Penrose, "Gravitational collapse and space-time singularities," Phys. Rev. Lett. **14** (1965), 57-59

[70] P. O. Mazur and E. Mottola, "Gravitational vacuum condensate stars," Proc. Nat. Acad. Sci. **101** (2004), 9545-9550 [arXiv:gr-qc/0407075 [gr-qc]].

[71] P. O. Mazur and E. Mottola, "Gravitational Condensate Stars: An Alternative to Black Holes," Universe **9** (2023) no.2, 88 [arXiv:gr-qc/0109035 [gr-qc]].

[72] R. Carballo-Rubio, F. Di Filippo, S. Liberati and M. Visser, "Geodesically complete black holes," Phys. Rev. D **101** (2020), 084047 [arXiv:1911.11200 [gr-qc]].

[73] R. Carballo-Rubio, F. Di Filippo, S. Liberati and M. Visser, "A connection between regular black holes and horizonless ultracompact stars," JHEP **08** (2023), 046 [arXiv:2211.05817 [gr-qc]].

[74] M. Cadoni, M. Oi and A. P. Sanna, "Effective models of nonsingular quantum black holes," Phys. Rev. D **106** (2022) no.2, 024030 [arXiv:2204.09444 [gr-qc]].

[75] D. Charbulák and Z. Stuchlík, "Spherical photon orbits in the field of Kerr naked singularities," Eur. Phys. J. C **78** (2018) no.11, 879 [arXiv:1811.02648 [gr-qc]].

[76] D. Charbulák and Z. Stuchlík, Eur. Phys. J. C **77** (2017) no.12, 897 doi:10.1140/epjc/s10052-017-5401-9 [arXiv:1702.07850 [gr-qc]].

[77] B. Nguyen, P. Christian and C. k. Chan, "Shadow Geometry of Kerr Naked Singularities," Astrophys. J. **954** (2023) no.1, 78 [arXiv:2302.08094 [astro-ph.HE]].

[78] E. G. Gimon and P. Horava, "Astrophysical violations of the Kerr bound as a possible signature of string theory," Phys. Lett. B **672** (2009), 299-302 [arXiv:0706.2873 [hep-th]].

[79] S. Hadar, M. D. Johnson, A. Lupsasca and G. N. Wong, "Photon Ring Autocorrelations," Phys. Rev. D **103** (2021) no.10, 104038 [arXiv:2010.03683 [gr-qc]].

[80] J. Levin and G. Perez-Giz, "Homoclinic Orbits around Spinning Black Holes. I. Exact Solution for the Kerr Separatrix," Phys. Rev. D **79** (2009), 124013 [arXiv:0811.3814 [gr-qc]].

[81] Y. T. Li, C. Y. Wang, D. S. Lee and C. Y. Lin, "Homoclinic orbits in Kerr-Newman black holes," Phys. Rev. D **108** (2023) no.4, 044010 [arXiv:2302.09471 [gr-qc]].

[82] F. D. Ryan, "Effect of gravitational radiation reaction on circular orbits around a spinning black hole," Phys. Rev. D **52** (1995), R3159-R3162 [arXiv:gr-qc/9506023 [gr-qc]].

[83] L. Barack and C. Cutler, "Using LISA EMRI sources to test off-Kerr deviations in the geometry of massive black holes," Phys. Rev. D **75** (2007), 042003 [arXiv:gr-qc/0612029 [gr-qc]].

[84] P. Amaro-Seoane, J. R. Gair, A. Pound, S. A. Hughes and C. F. Sopuerta, "Research Update on Extreme-Mass-Ratio Inspirals," J. Phys. Conf. Ser. **610** (2015) no.1, 012002 [arXiv:1410.0958 [astro-ph.CO]].

[85] G. V. Kraniotis, "Gravitational redshift/blueshift of light emitted by geodesic test particles,

frame-dragging and pericentre-shift effects, in the Kerr–Newman–de Sitter and Kerr–Newman black hole geometries," Eur. Phys. J. C **81** (2021) no.2, 147 [arXiv:1912.10320 [gr-qc]].

[86] P. Jai-akson, A. Chatrabhuti, O. Evnin and L. Lehner, "Black hole merger estimates in Einstein-Maxwell and Einstein-Maxwell-dilaton gravity," Phys. Rev. D **96** (2017) no.4, 044031 [arXiv:1706.06519 [gr-qc]].

[87] N. Tsukamoto, Z. Li and C. Bambi, "Constraining the spin and the deformation parameters from the black hole shadow," JCAP **06** (2014), 043 [arXiv:1403.0371 [gr-qc]].

[88] N. Tsukamoto, "Black hole shadow in an asymptotically-flat, stationary, and axisymmetric spacetime: The Kerr-Newman and rotating regular black holes," Phys. Rev. D **97** (2018) no.6, 064021 [arXiv:1708.07427 [gr-qc]].